



Seismic Velocity Structure of Central Asia from Surface-Wave Dispersion

Brett Ketter, B.S.

A Thesis Presented to the Faculty of the Graduate School of Saint Louis University
in Partial Fulfillment of the Requirements for the Degree of
Master of Science (Research)

COMMITTEE IN CHARGE OF CANDIDACY

Associate Professor Charles J. Ammon,
Chairperson and Advisor

Professor Robert B. Herrmann

Professor Brian J. Mitchell

This thesis is dedicated to my fiancé,

Jenny

who could light the darkest of days with a smile or a touch.

ACKNOWLEDGEMENTS

I would like to thank my advisor, Dr. Charles J. Ammon, for his insight and guidance on this project. I would also like to thank Aaron Velasco, Howard Patton and George Randall at Los Alamos National Laboratory for their patience with me during the beginning stages of this project and allowing me the freedom to try explore new ideas. I appreciate the careful review of this manuscript by Dr. Robert Herrmann and Dr. Brian Mitchell. Finally, thanks to my friend Rommel Villagomez who helped me understand more than just science throughout my graduate career.

This research was sponsored by U.S. Department of Energy, Office of Nonproliferation and National Security, Office of Research and Development, Contract No. W-7405-ENG-36.

TABLE OF CONTENTS

COMMITTEE IN CHARGE OF CANDIDACY	ii
ACKNOWLEDGEMENTS	iv
TABLE OF CONTENTS	v
LIST OF FIGURES	vii
LIST OF TABLES	x
INTRODUCTION	1
Overview	1
THE GEOLOGY OF CENTRAL ASIA	4
Regional Tectonics	4
Geology of the Tien Shan	5
Geology of the Tibetan Plateau	8
Geology of the Tarim Basin	8
Geology of the Junggar Basin	9
GEOPHYSICAL INVESTIGATIONS OF CENTRAL ASIA	10
Gravity Variations in Central Asia	10
Seismic Refraction/Reflection in Central Asia	12
ESTIMATES OF VELOCITY STRUCTURE OF CENTRAL ASIA FROM SURFACE AND BODY WAVES	13
Surface-Wave and Body-Wave Investigations of Central Asia	13
Receiver Function Analysis of Central Asia	17
SURFACE-WAVE DISPERSION ANALYSIS	19

Earthquakes and Stations	19
Surface Waves	19
Group Velocity Measurement	22
Phase-Velocity Measurement	25
Path Averaging	28
Sources of Uncertainty	33
Estimating Earth Structure using Surface Wave Dispersion	46
Damping Parameters for Shear-Velocity Inversion	47
SEISMIC SHEAR-VELOCITY VARIATIONS OF CENTRAL ASIA	49
Shear Velocity for the Junggar Basin Path	49
Shear Velocity for the Tibet Plateau-Tarim Basin Path	54
Shear Velocity for the Tarim-Tien Shan Path	54
CONCLUSIONS	62
PARAMETERS FOR FINAL SHEAR-VELOCITY MODELS	65
BIBLIOGRAPHY	67
VITA AUCTORIS	70

LIST OF FIGURES

- Figure 1.1.1. Regional map of central Asia showing geologic features, the earthquakes (purple circle) and stations (yellow triangles). The bold star indicates Lop Nor, the Chinese nuclear test site. The rectangle identifies the study area, plotted in Figure 1.1.2. 2
- Figure 1.1.2. Expanded map of the study area showing the earthquake locations (purple circles), focal mechanisms (orange circles) and stations (yellow triangles). The bold star indicates Lop Nor, the Chinese nuclear test site. 3
- Figure 2.1.1. Map of central Asia showing major faults and structural provinces. 6
- Figure 2.1.2. Proposed model to explain the transmission of stresses in central Asia. Dashed line indicates weak coupling between crust and upper mantle. Tibet is moving out of the picture in bottom drawing (redrawn from Molnar and Tapponnier, 1979). 7
- Figure 3.1.1. Region map showing locations of previous studies of central Asia. MP1 = Mahdi and Pavlis (1998) eastern Tien Shan path; MP2 = Mahdi and Pavlis Tarim-Tien Shan path; MP3 = Mahdi and Pavlis Turan Tien Shan path; CA1 = Cotton and Avouac (1994) eastern Tien Shan path; CA2 = Cotton and Avouac central Tien Shan path; R = Romanowicz (1982) Tibet path; RS = Roecker et al. (1993) central Tien Shan; BEL = Belousov et al. (1980) refraction/reflection survey line; BUR = Burov et al., (1990) gravity profiles. Rectangle shows approximate location of Vinnik and Saipbektova (1984) 2-D and Ghose et al. (1998) 3-D tomographic investigations of central Asia. 11
- Figure 4.1.1. Models from previous studies: MP1 = Mahdi and Pavlis (1998) eastern Tien Shan path; MP2 = Mahdi and Pavlis Tarim-Tien Shan path; MP3 = Mahdi and Pavlis Turan Tien Shan path; CA1 = Cotton and Avouac (1994) central Tien Shan path; CA2 = Cotton and Avouac eastern Tien Shan path; R = Romanowicz (1982) Tibet path (from phase velocities); RS = Roecker et al. (1993) central Tien Shan; ASIA = Kosarov et al. (1993) and Patton (1998); M = Moho depth. 15
- Figure 5.3.1. Vertical component seismogram from the March 19, 1996 event at station Nilore, Pakistan. The top panel is the raw data seismogram, the middle panels show the rotated seismogram, and the bottom is the phase matched-filtered seismogram from the program SWMFA. 23
- Figure 5.3.2. Output from SWMFA, including spline-fit dispersion curve, velocity amplitude, and spectral amplitude (left to right, respectively). 24
- Figure 5.3.3. Observed (dots) and average (solid line) Love-wave group velocities. Dots are the observed Love-wave group velocities at each period. Solid line is the calculated mean for all 26 events. 26
- Figure 5.3.4. Observed (dots) and average (solid line) Rayleigh-wave group velocities. Dots are the

observed Rayleigh-wave group velocities at each period. Solid line is the calculated mean for all 26 events.	27
Figure 5.4.1. Phase velocity output from the March 19, 1996 earthquake recorded at MAK. Circles and triangles indicate reference velocity dispersion curves. Squares indicate estimated group velocity curve. Lines spreading out are the 2pN uncertainties introduced into the phase calculation. The correct branch of 2pN is chosen (N = +1) on how it fits the reference curves.	29
Figure 5.4.2. Observed (dots) and average (solid line) Love-wave phase velocities. Dots are the observed Love-wave phase velocities at each period. Solid line is the calculated mean for all 26 events.	30
Figure 5.4.3. Observed (dots) and average (solid line) Rayleigh-wave phase- velocities. Dots are the observed Rayleigh-wave phase velocities at each period. Solid line is the calculated mean for all 26 events	31
Figure 5.5.1. Region map showing locations of average phase velocity paths used in the inversions. See figure 1.1.1 for explanation of map symbols.	32
Figure 5.5.2. Observed Love-wave group-velocities with calculated standard deviations for the Junggar path.	34
Figure 5.5.3. Observed Rayleigh-wave group-velocities with calculated standard deviations for the Junggar path.	35
Figure 5.5.4. Observed Love-wave phase-velocities with calculated standard deviations for the Junggar path.	36
Figure 5.5.5. Observed Rayleigh-wave phase-velocities with calculated standard deviations for the Junggar path.	37
Figure 5.5.6. Observed Love-wave group-velocities with calculated standard deviations for the Tibet-Tarim path.	38
Figure 5.5.7. Observed Rayleigh-wave group-velocities with calculated standard deviations for the Tibet-Tarim path.	39
Figure 5.5.8. Observed Love-wave phase-velocities with calculated standard deviations for the Tibet-Tarim path.	40
Figure 5.5.9. Observed Rayleigh-wave phase-velocities with calculated standard deviations for the Tibet-Tarim path.	41
Figure 5.5.10. Observed Love-wave group-velocities with calculated standard deviations for the Tarim-Tien Shan path.	42

Figure 5.5.11. Observed Rayleigh-wave group-velocities with calculated standard deviations for the Tarim-Tien Shan path	43
Figure 5.5.12. Observed Love-wave phase-velocities with calculated standard deviations for the Tarim-Tien Shan path	44
Figure 5.5.13. Observed Rayleigh-wave phase-velocities with calculated standard deviations for the Tarim-Tien Shan path.	45
Figure 6.1.1. Inversion results for the Asia model of Patton (1998) for the Junggar Basin path. The top panel shows the final model and resolution kernels. The bottom diagrams show the fit of the observations to the predicted model. The top curve in each bottom diagram is the phase velocity fit to the model and the bottom is the group velocity fit (Rayleigh and Love).	51
Figure 6.1.2. Inversion results for the Mahdi and Pavlis (1998) model for the Junggar path. See Figure 6.1.1 for explanation.	52
Figure 6.1.3. Inversion results for the Roecker et al. (1993) M1 model for the Junggar path. See Figure 6.1.1 for explanation.	53
Figure 6.2.1. Inversion results for the Asia model of Patton (1998) for the Tibet-Tarim Basin path. See Figure 6.1.1 for explanation.	55
Figure 6.2.2. Inversion results for the Mahdi and Pavlis (1998) model for the Tibet-Tarim Basin path. See Figure 6.1.1 for explanation.	56
Figure 6.2.3. Inversion results for the Roecker et al. (1993) M1 model for the Tibet-Tarim Basin path. See Figure 6.1.1 for explanation.	57
Figure 6.3.1. Inversion results for the Asia model of Patton (1998) for the Tarim-Tien Shan path. See Figure 6.1.1 for explanation.	58
Figure 6.3.2. Inversion results for the Mahdi and Pavlis (1998) model for the Tarim-Tien Shan path. See Figure 6.1.1 for explanation.	59
Figure 6.3.3. Inversion results for the Roecker et al. (1993) M1 model for the Tarim-Tien Shan path. See Figure 6.1.1 for explanation.	60
Figure 7.0.1. Final shear velocity models using the WMQ observations for the three paths. Only the upper 20 km is shown to illustrate resolution in the upper crust. The Tarim-Tien Shan and Tibet-Tarim Basin paths fit best with the Mahdi and Pavlis (1998) model; the Junggar Basin path fits best with the M1 model of Roecker et al. (1993).	63

LIST OF TABLES

Table 1 List of Stations Used in the Study	20
Table 2 List of Events Used in the Study	21
Table 3 Change in epicenter location and its affect on phase velocity.	46
Table 4 Parameters for Junggar Path Inversions	50
Table 5 Parameters for Tibet-Tarim Path Inversions	54
Table 6 Parameters for Tarim-Tien Shan Path Inversions	61
Table 7 Final Shear-Velocity Model for the Tarim-Tien Shan Path	65
Table 8 Final Shear-Velocity Model for the Tibet-Tarim Basin Path	66
Table 9 Final Shear-Velocity Model for the Junggar Basin Path	66

CHAPTER 1 INTRODUCTION

1.1 Overview

Geologic complexity in central Asia is the direct result of the collision of India with Asia that began in the Eocene (~50 Ma) and continues today. The collision has created some of the most pronounced topography in the world. The Tibetan Plateau has a mean elevation of 5000 m and is the largest plateau in the world. The Tien Shan Mountains rise to a maximum height of 7000 m and are one of the furthest mountain ranges from an active convergent plate boundary. Among the elevated regions are several large basins including the Tarim and Junggar (Figure 1.1.1) that filled with thousands of meters of sediments eroded from elevated terrain. As expected, this actively deforming region has many earthquakes but are mostly confined to the Tien Shan Mountains, only sporadic activity occurs in the basins.

This region of young, rugged geology is not without political interest. Lop Nor, the Chinese nuclear test site, is located (Figure 1.1.2) just north of the Tarim basin and is the site of numerous underground nuclear explosions (the last known in 1996). One specific goal of this study is to map the seismic velocity variations along known source-receiver paths that will improve our ability to investigate small nuclear explosions in the Lop Nor region.

To study velocity variations, Rayleigh and Love waves were analyzed to estimate surface-wave group and phase velocity dispersion for known propagation paths. Group velocities were estimated using a multiple-filter method and isolating the surface-wave for phase velocity estimation. The group velocity estimates agree with previous surface-wave studies of central Asia. Phase velocity estimates were calculated for the 26 events using the single-station method and assuming source phase corrections from available moment-tensor and depth estimates. To reduce the data, the earthquakes are grouped into three clusters and the phase velocities of each cluster are averaged. Finally, the average phase and group velocity dispersion along each path were used to estimate a depth dependent shear wave velocity structure. The results are consistent with previous work.

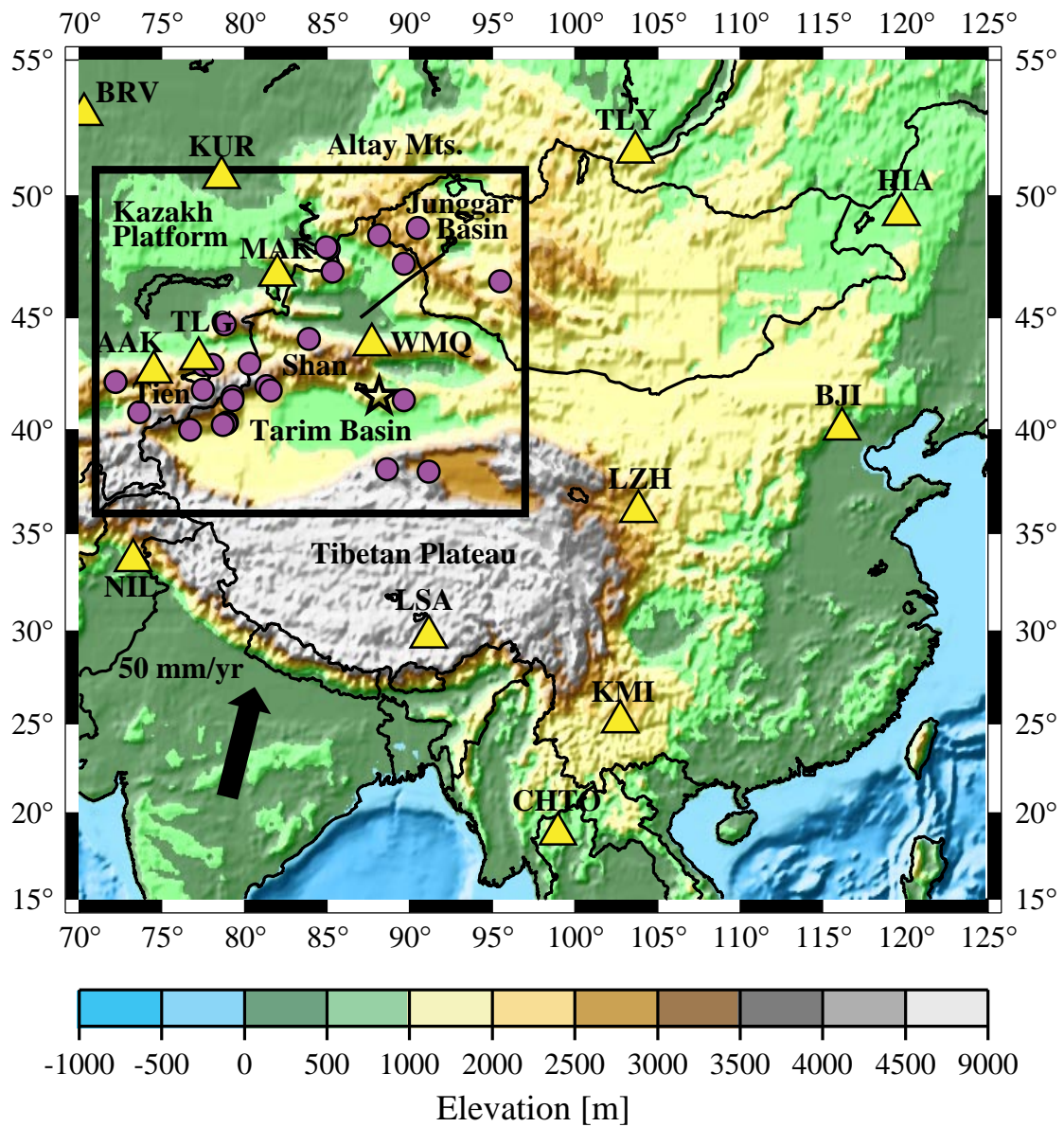


Figure 1.1.1. Regional map of central Asia showing geologic features, the earthquakes (purple circle) and stations (yellow triangles). The bold star indicates Lop Nor, the Chinese nuclear test site. The rectangle identifies the study area, plotted in Figure 1.1.2.

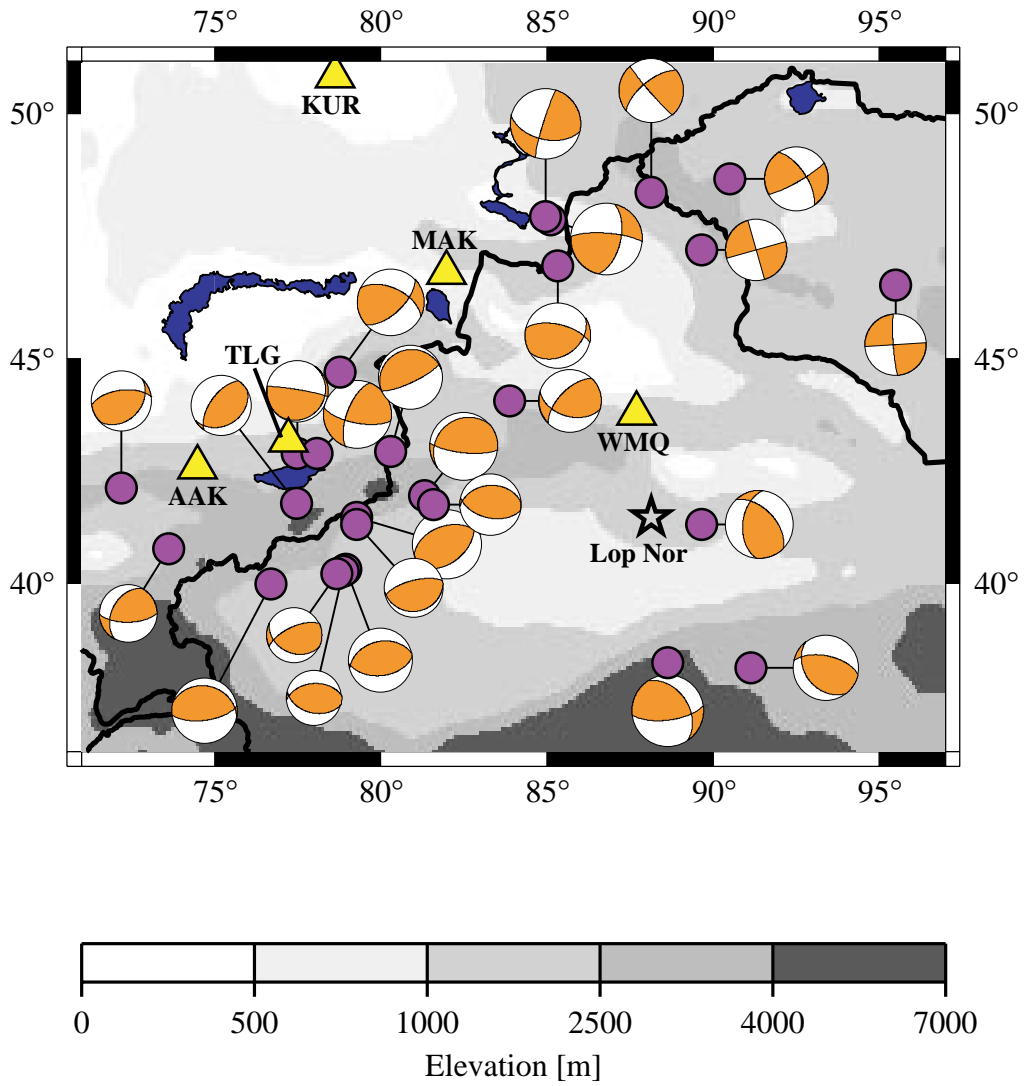


Figure 1.1.2. Expanded map of the study area showing the earthquake locations (purple circles), focal mechanisms (orange circles) and stations (yellow triangles). The bold star indicates Lop Nor, the Chinese nuclear test site.

CHAPTER 2 THE GEOLOGY OF CENTRAL ASIA

2.1 Regional Tectonics

Central Asia is the culmination of several tectonic episodes involving collisions of numerous small crustal blocks since the Precambrian. These blocks include the Tien Shan, Tibet, the Tarim Basin, and the Junggar basin. Each of the blocks was accreted by the end of the Paleozoic; later tectonic events further changed the geologic and kinematic characteristics of central Asia.

Central Asia is seismically active including several events with $M_S > 8.0$ since the beginning of this century (Nelson et al., 1987). Tapponnier and Molnar (1979) and Ni (1978) used LANDSAT imagery and earthquake fault plane solutions to interpret active tectonics in central Asia. Formation of the Tien Shan Mountains began in the late Paleozoic but the area was reduced to an elevated plain until the Eocene when deformation was reactivated as a result of the India-Eurasia collision 1500 km to the south (Zonenshain et al., 1990; see arrow on Figure 1.1.1). Northward convergence of India into Eurasia thickened the crust by thrusting and folding of the Tien Shan (Tapponnier and Molnar, 1979; Avouac et al., 1993). Fault plane solutions are consistent with the predicted convergence of India into Eurasia with crustal shortening estimated at $\sim 200 \pm 50$ km since the initial collision (Avouac et al., 1993). Molnar and Deng (1984) summed seismic moments from four earthquakes ($M > 7.5$) and estimated a rate of shortening across the Tien Shan of 13 ± 7 mm/yr. Avouac et al., (1993) showed crustal shortening produces a clockwise rotation ($7 \pm 2.5^\circ$) of the Tarim Basin relative to Kazakh Platform and Junggar Basin since the Cenozoic.

Nelson et al. (1987) used P and SH waveforms from 11 Tien Shan earthquakes to constrain the earthquake fault plane solutions and depths for thrust faulting events with depths from 10 to 44 km and body wave magnitudes from 5.5 to 6.2. Relocated earthquakes and focal mechanisms also indicate north-northwest to north-northeast shortening. The earthquakes appear to rupture along range-bounding faults that dip $33\text{-}35^\circ$ beneath the mountains (Nelson et al., 1987). Range-bounding faults account for the uplifted basement blocks with thrust faults on the north and south side of the range giving the Tien Shan Mountains its height.

Although thrust faulting is prevalent in central Asia, there are large-scale right lateral strike-slip faults that strike perpendicular to the Tien Shan and appear to die out within the Kazakh and Sibe-

rian platforms (Tapponnier and Molnar, 1979; Figure 2.1.1). The Talasso-Fergana fault has about 250 km of right-lateral offset since the late Paleozoic and serves as a thermal and seismic boundary between the two blocks of the Tien Shan (Ni, 1978; Vinnik and Saipbektova, 1984; Kosarov et al., 1993, Roecker et al., 1993; Figure 2.1.1). A gradual change from thrust faulting at high altitudes of the Tien Shan to strike-slip faulting toward the Junggar Basin reflects the change in stress conditions that are present in this region. Near the Junggar Basin, left-lateral strike-slip faulting accommodates deformation caused by the impinging Indian continent (Tapponnier and Molnar, 1979). The combination of thrust faults and right and left-lateral strike-slip faults is responsible for the pattern of basins surrounded by high mountain ranges (Tapponnier and Molnar, 1979).

East-west extension along normal faults dominates the tectonics of Tibet, despite deformation in the rest of Asia being dominated by north-south compression (Tapponnier and Molnar, 1977; Molnar and Tapponnier, 1978). Normal faulting is limited to areas with the highest mean elevation and form grabens that fill with sediments. Along the northern edge of the Tibetan Plateau, the Altyn Tagh left-lateral fault accommodates stress from the India-Eurasia collision allowing Tibet to slip to the northeast.

Molnar and Tapponnier (1978) proposed a model of India moving north into the Siberian block, deforming the region between them (Figure 2.1.2). In the model, Siberia, Tarim and India act as a rigid block and Tibet as a contained fluid. Tibet is underlain by weak material and the collision of India maintains the high elevations of Tibet. Thus Tibet is a pressure gauge of Asia and transmits the collision stresses to regions to the north and east (Molnar and Tapponnier, 1978). Tibet transmits stresses to the Tarim Basin, which acts as a rigid block thus causing crustal thickening in the Tien Shan along range-bounding faults. Thrust faulting is not currently contracting Tibet; east-west strike-slip faulting and north-south normal faulting absorb the collision stresses allowing Tibet to “slide” to the east (Molnar and Tapponnier, 1978).

2.2 Geology of the Tien Shan

The Tien Shan is composed of E-W trending mountain ranges cored by Precambrian to early Paleozoic crystalline basement rock separated by basins filled with Cenozoic synorogenic sediments (Figure 2.1.1). The mountains stretch from east to west for more than 2000 km, and reach eleva-

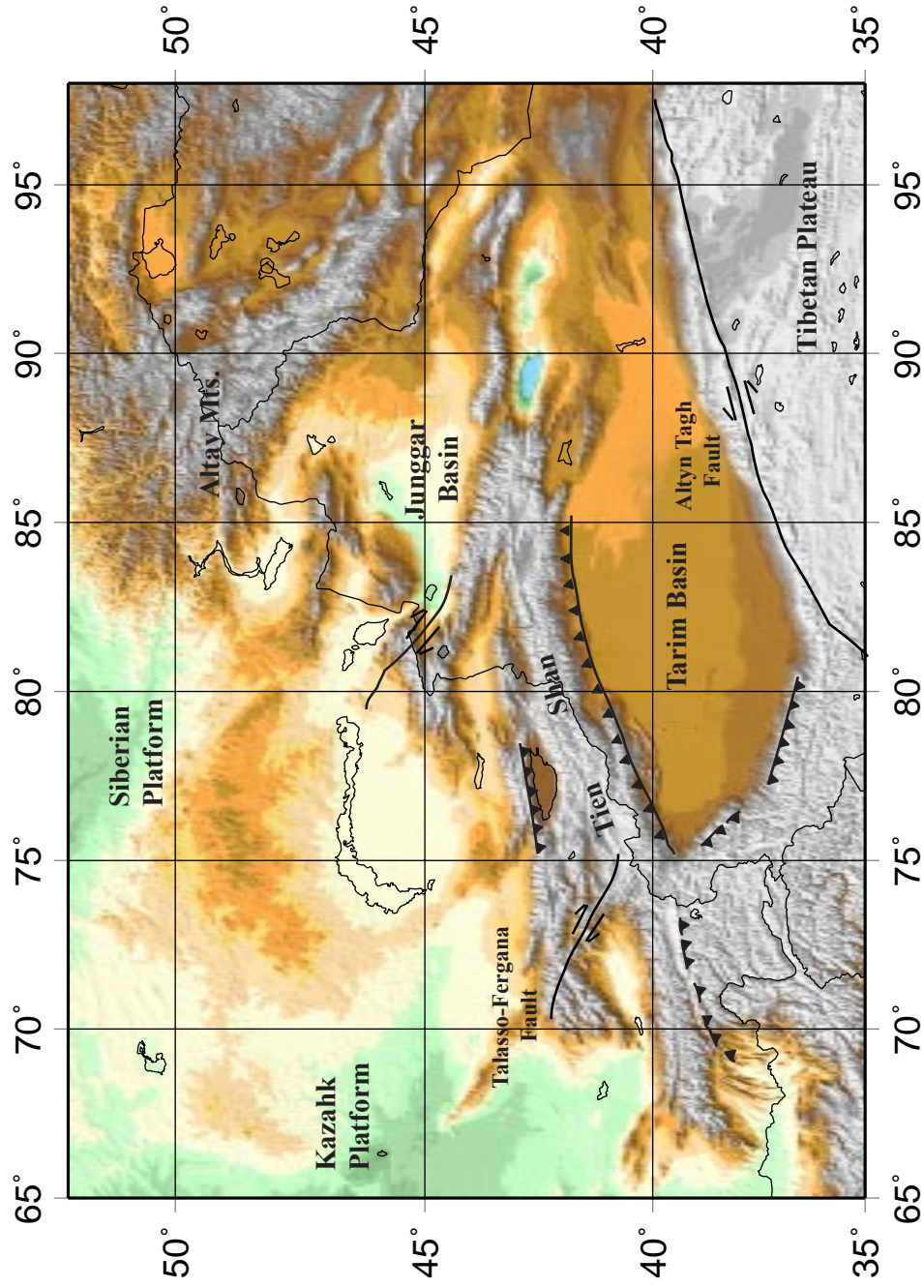


Figure 2.1.1. Map of central Asia showing major faults and structural provinces.

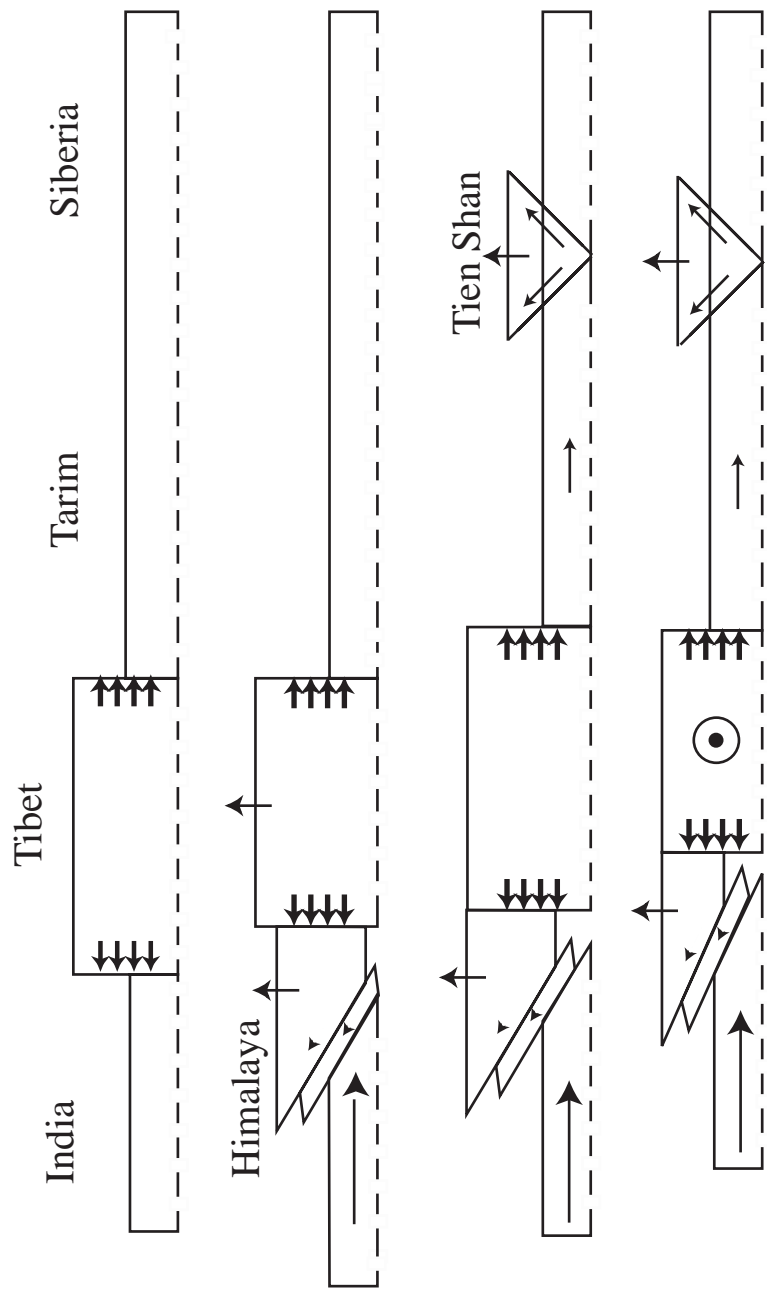


Figure 2.1.2. Proposed model to explain the transmission of stresses in central Asia. Dashed line indicates weak coupling between crust and upper mantle. Tibet is moving out of the picture in bottom drawing (redrawn from Molnar and Tappanier, 1979).

tions of over 7000 m separated by basins with elevations of 2000-3000 m. A Precambrian collision between an ancient fragment and the Siberian Platform produced a fold belt (Zonenshain, 1990). Precambrian foldbelt rocks of the Tien Shan consist of gniesses and greenstone belts that range in age from 1800 Ma to 1900 Ma and sandstones that transformed into quartzites that range in age from 1100 Ma to 900 Ma (Zonenshain, 1990). Early Paleozoic ophiolite sutures separate the small Precambrian blocks and consist of ultramafic rocks, gabbros, and pillow lavas with isotope ages that range from 1270 Ma to 680 Ma (Zonenshain, 1990). An ancient sea once covered central Asia which deposited Ordovician platform sediments that lie unconformably over Proterozoic basement rock followed by deep marine shale sediments (Coleman, 1989). Throughout the rest of the Paleozoic, volcanoclastics, and deep marine shales were deposited and subsequently compressed by the collision of India with Eurasia, thickening the crust (Molnar and Tapponnier, 1975; Coleman, 1989).

2.3 Geology of the Tibetan Plateau

The Tibetan plateau is a large (1000 km x 1700 km) roughly triangular block with a mean elevation of 5000 m (Figure 1.1.1). Tibet formed by the accretion of continental and/or island arc fragments between the late Paleozoic and middle Cretaceous (Molnar and Tapponnier, 1978). Late Cretaceous shallow marine sediments were deposited prior to the collision of India with Asia when the Tibetan plateau was probably at lower elevations seen. These same sediments provide constraint on timing of the India-Eurasia collision. The late Cretaceous sediments form the top of the uplifted Tibetan block; therefore the initial collision must have occurred in the Cenozoic (Molnar and Tapponnier, 1978).

Cenozoic volcanism is prevalent in Tibet and consists of calc-alkaline rocks such as andesites, dacites, and latites (Molnar and Tapponnier, 1978). Widespread volcanism, low seismic velocities and high attenuation provide evidence from a 'hot' mantle beneath Tibet (Molnar and Tapponnier, 1978; Chen and Molnar, 1978). Cenozoic sediments fill the numerous grabens formed by normal faulting.

2.4 Geology of the Tarim Basin

The Tarim Basin is an elliptical-shaped block located between the Tien Shan to the north and the Tibetan block to the south (Figure 2.1.1). Precambrian basement rocks are only located at the

periphery of the basin and consist of schist, fossil-bearing marble and quartzite. Tightly folded and metamorphosed rocks consolidated in the Late Proterozoic to form the nucleus of the Tarim Basin (Zhang et al., 1984; Coleman, 1989). Early Paleozoic clastics, tillites, and volcanics lie unconformably over the basement rocks followed by Late Paleozoic marine clastics and carbonates (Zhang et al., 1984). Apparent polar wander paths show the Tarim block collided with the already consolidated Eurasian blocks by the end of the Permian (Li, 1990). Finally, Mesozoic-Cenozoic rocks of gypsum-bearing red beds cover the top of the Tarim Basin (Zhang et al., 1984). A transgressive sedimentary sequence along the western part of the Tarim Basin produced some oil-bearing rocks. Compression from the India-Eurasia collision caused uplift and subsidence of fault blocks and forced older strata over Tertiary deposits forming overturned folds in the Tarim Basin (Huang et al., 1987). The Tarim Basin is nearly devoid of any seismic activity.

2.5 Geology of the Junggar Basin

The Junggar Basin is located south of the Altay Mountains and north of the Tien Shan Mountains and was accreted to the Kazakhstan Block in the early to middle Paleozoic (Li, 1984; Figure 2.1.1). Basement rocks underneath the Junggar Basin do not outcrop, but may be a mafic basement remnant of a trapped ocean basin from the Paleozoic that show strong magnetic anomalies (Coleman, 1989; Carroll et al., 1990). The oldest exposed rocks in the Junggar Basin date to the Middle Ordovician and consist of limestone, calcareous sandstone, tuff, andesite, and reef limestone with a total thickness of 3-4 km (Huang et al., 1987; Carroll et al., 1990). Lead isotope dates on Middle Carboniferous granites (321.4 ± 6.7 Ma) suggest they derived from partial melting of oceanic material (Coleman, 1989; Carroll et al., 1990). Lower Carboniferous strata include unconformities as a result of several tectonic movements during this time. Tectonic movements formed narrow zones of alternating sediments with volcanic material and sediments with clastic and limestone materials (Huang et al., 1987). Deposits covering the Junggar Basin consist of terrestrial clastic rocks derived from the Tien Shan and Altay Mountains.

CHAPTER 3 GEOPHYSICAL INVESTIGATIONS OF CENTRAL ASIA

Since the 1950's, central Asia has been the focus of many geophysical investigations. Seismic investigations provide information about the variations in seismic velocities to determine a suitable crustal structure model and help explain the dynamic processes taking place in central Asia. Gravity studies show the distribution of density contrasts and show if the region is in isostatic equilibrium. I review studies that are pertinent to enhancing the overall picture of how surface-wave energy propagates beneath central Asia with particular emphasis on those investigations, which provide models of seismic velocity variations with depth in central Asia.

3.1 Gravity Variations in Central Asia

Active convergence in an intercontinental mountain belt manifests itself geologically by crustal thickening over a wide zone of thrust faults (Burov et al., 1989). Thickening of the upper crust beneath the belt should form a lithospheric root beneath the mountain chain and is explained by an Airy isostatic model. High elevations (thick crust) stay in equilibrium by “sitting” lower in the higher density mantle material thus creating a lithospheric root to the mountain chain. Burov et al. (1989) examined central Asia Bouguer gravity anomalies and how the deep structure beneath the Tien Shan differs from the surrounding region. Figure 3.1.1 show the location of three of the gravity profiles. Western Tien Shan Bouguer gravity anomalies measure within 10 mgal of values necessary for Airy isostatic equilibrium (Burov et al., 1989), but eastern Tien Shan gravity anomalies are negative and almost 50 mgal too small. The small differences in the western Tien Shan indicate much of the lithosphere here is in isostatic equilibrium. However, large deviations from the local isostatic equilibrium (~50 mgal) implies the dynamic processes taking place in the Tien Shan Mountains varies along the chain.

Burov et al., (1989) proposed two hypotheses to explain the large negative values. First, a deep mass of thickened crust may underlie the eastern part of the range and second, normal stresses resulting from the flow in the asthenosphere, may pull the Tien Shan down. The actual may be a combination of the two hypotheses, allowing sinking of the thickened lithospheric root from flow in the asthenosphere, causing deepening of the Moho and creating negative gravity anomalies.

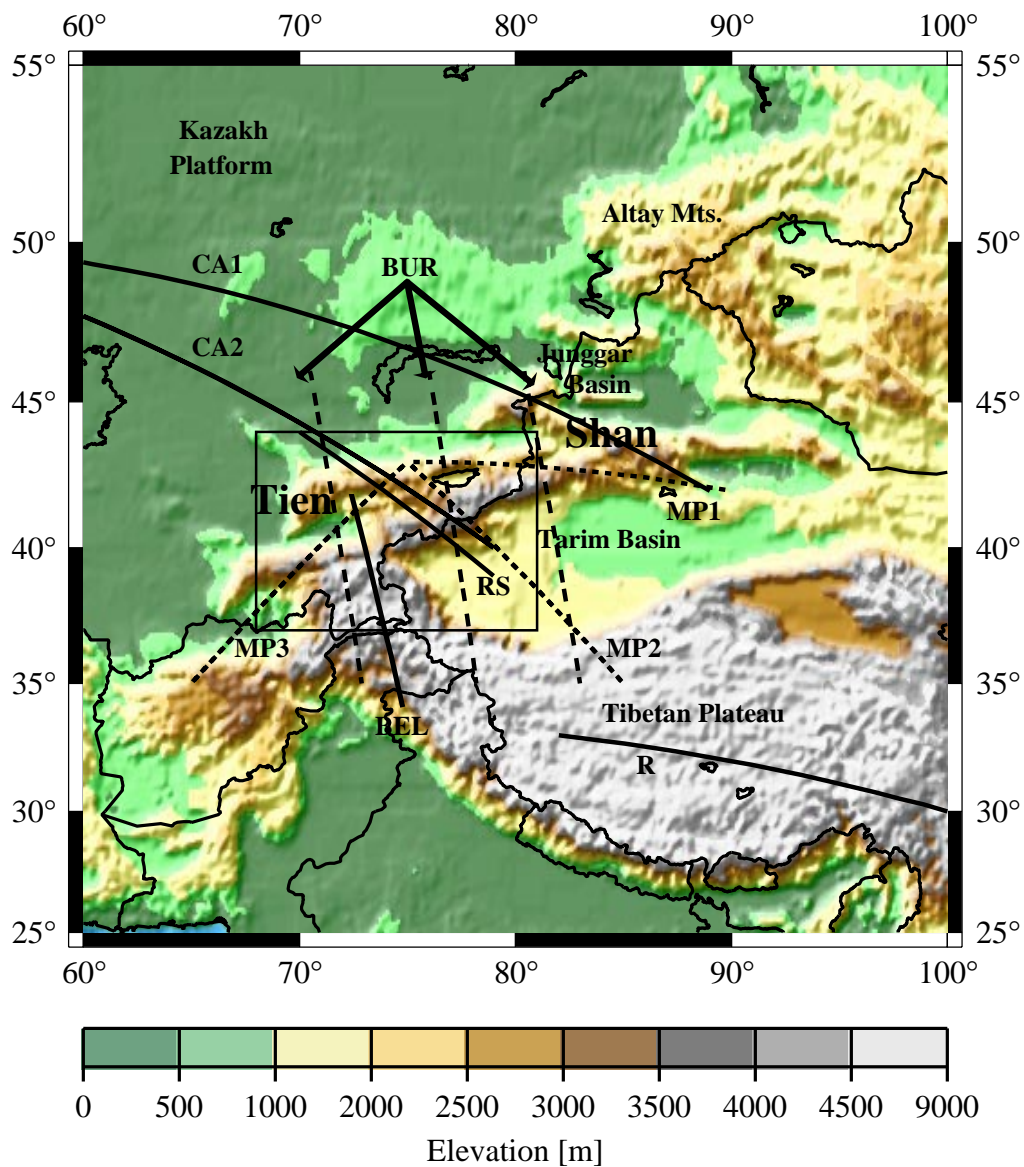


Figure 3.1.1. Region map showing locations of previous studies of central Asia. MP1 = Mahdi and Pavlis (1998) eastern Tien Shan path; MP2 = Mahdi and Pavlis Tarim-Tien Shan path; MP3 = Mahdi and Pavlis Turan Tien Shan path; CA1 = Cotton and Avouac (1994) eastern Tien Shan path; CA2 = Cotton and Avouac central Tien Shan path; R = Romanowicz (1982) Tibet path; RS = Roecker et al. (1993) central Tien Shan; BEL = Belousov et al. (1980) refraction/reflection survey line; BUR = Burov et al., (1990) gravity profiles. Rectangle shows approximate location of Vinnik and Saipbektova (1984) 2-D and Ghose et al. (1998) 3-D tomographic investigations of central Asia.

An elastic plate over an inviscid fluid and loaded by the weight of the overlying topography best explains the 10-20 mgal Bouguer gravity anomalies (Burov et al., 1989). Typical densities for the model include 3300 kg/m³ for the mantle and 2670 kg/m³ for crustal rocks and unconsolidated sediments. To create the large negative anomaly beneath the Tien Shan, the best model yielded a flexural rigidity value for the theoretical plate of 1023 Nm and a thickness of 25 km (Burov et al., 1989). Beneath the Tarim Basin, theoretical plate rigidity of 1024 Nm with a thickness of 50-60 km recreated the observed Bouguer anomalies.

3.2 Seismic Refraction/Reflection in Central Asia

As part of the International Geodynamic Project, Belousov et al., (1980), performed a deep refraction/reflection survey across the Tien Shan-Pamirs-Karakorum-Himalaya region. Refraction and reflection profiles using large borehole explosions provided a good picture of the regional geologic structure. Figure 3.1.1 shows the location of the refraction/reflection profile. Time-versus-distance curves at distances of 100-120 and over 250 km were made from refracted P-wave and P_n first arrivals, respectively. At these distances, velocities correspond to upper consolidated crustal rocks. At distances between 120 and 250 km, the P-wave is reflected off the Moho. Results from Belousov et al., (1980) show a 9-10 layer of sedimentary cover. Crustal rocks are 35-37 km thick beneath the Tien Shan with compressional velocities that range from 6.0 to 6.7 km/s to the top of the Moho at 55 km. In addition they found that the depth to the top of the asthenosphere is typically 120 km beneath the Tien Shan that thickness decreases to the north and south.

CHAPTER 4 ESTIMATES OF VELOCITY STRUCTURE OF CENTRAL ASIA FROM SURFACE AND BODY WAVES

4.1 Surface-Wave and Body-Wave Investigations of Central Asia

Cotton and Avouac (1994) used surface-wave dispersion to examine the crustal and upper mantle structure under the Tien Shan. Figure 3.1.1 gives the location of the paths used in their inversion (marked CA1 and CA2). Earthquakes and nuclear explosions in central Asia recorded at three stations in France are examined to estimate the group velocity dispersion for each path. They analyzed 18 fundamental mode Rayleigh waves obtained from vertical component records with periods ranging from 15 to 70 seconds. Mean group velocities for each path have estimated errors less than 0.03 m/sec.

A one-dimensional inversion performed with the observed group velocities shows a crust approximately 50-55 km thick. Although periods below 15 seconds are observed, those below 25 seconds are not reliable; therefore resolution in the upper crust is nominal at best. Their best-fitting model for the central Tien Shan includes a 50 km crust with a shear-wave velocity of about 3.7 km/sec, a mantle velocity of about 4.5 km/sec, and a low-velocity zone between 85 and 135 km with a shear-wave velocity around 4.0 km/sec. Eastern Tien Shan has a best-fitting model that includes a 55 km crust with a shear velocity of about 3.2 km/sec, a mantle velocity of about 5.2 km/sec, and a pronounced low-velocity zone between 110 and 155km with a velocity of about 4.4km/sec. Cotton and Avouac (1994) interpret the models and find no significant differences in the geodynamical processes taking place beneath the central and eastern Tien Shan. They conclude that north-south crustal shortening in the Cenozoic is responsible for the high topography (thick crust) in the Tien Shan.

Mahdi and Pavlis (1998) presented a regional surface wave study that incorporated earthquakes and explosions recorded by a local broadband seismic network to investigate the shear wave velocity structure of central Asia. They analyzed Rayleigh waves with periods from 3 to 50 seconds, generated by nine shallow earthquakes and four nuclear explosions. Grouping the earthquakes into three separate paths, Mahdi and Pavlis use average group-velocity dispersion from each path to estimate the one-dimensional shear velocity structure in the crust and upper mantle

for each of the three paths. The locations of the propagation paths used in the inversion are in Figure 3.1.1. The first path is from the west and south across the western Tarim Basin, next is the path across the eastern Tarim Basin, and finally the path from explosions at the Lop Nor test site.

A 4.0 km half-space with a fixed Poisson's ratio at 0.25 for the crust and 0.27 for the mantle is used as the initial model in the inversion. Upper mantle velocities along the Tien Shan path were well resolved because of the inclusion of higher mode data in the inversion. Models for the three paths consist of mainly four layers of increasing shear velocities with depth. The layers consist of: a low-velocity near-surface layer (~2.7 km/sec); an upper crust layer with a velocity of 3.5 km/sec; a lower crustal layer with velocities around 3.8 km/sec; and an upper mantle layer with a velocity around 4.5 km/sec (Mahdi and Pavlis, 1998). Results from this study revealed crustal thickness varying from 50 to 60 km, consistent with previous studies (Roecker et al., 1993, Cotton and Avouac, 1994).

Romanowicz (1982) examined the pure path phase velocities of Love and Rayleigh waves between 30 and 90 seconds across the Tibetan Plateau (Figure 3.1.1). Rayleigh wave phase velocity estimates ranged from 3.2 to 4.0 km/sec. A two-station method was performed where the stations lie on the same great circle path of the teleseismic event and align to within one degree. The best fitting model for the Tibetan paths had a 65 km thick crust, with an average shear-velocity of 4.65 km/sec. A low velocity zone was found between 100 and 150 km with phase velocities around 4.4 km/sec. Figure 4.1.1 compares the previous studies mentioned to illustrate the variation in crustal thickness in central Asia.

Vinnik and Saipbetkova (1984) used P-wave travel time residuals from distant earthquakes and P wave arrival times from local industrial explosions to image the two-dimensional velocity structure of the upper mantle beneath the Tien Shan (Figure 3.1.1). Results show two distinct provinces in the Tien Shan. Positive travel-time residuals and lower velocities in the eastern Tien Shan correlates with high elevations. Here, the residuals may be related to the thermal processes taking place in the upper mantle. The western Tien Shan travel-time residuals are negative and the velocities are higher, typical for stable platforms with a cold mantle. Mantle processes cannot explain the negative travel-time residuals.

Velocity Variations in Central Asia from Previous Studies

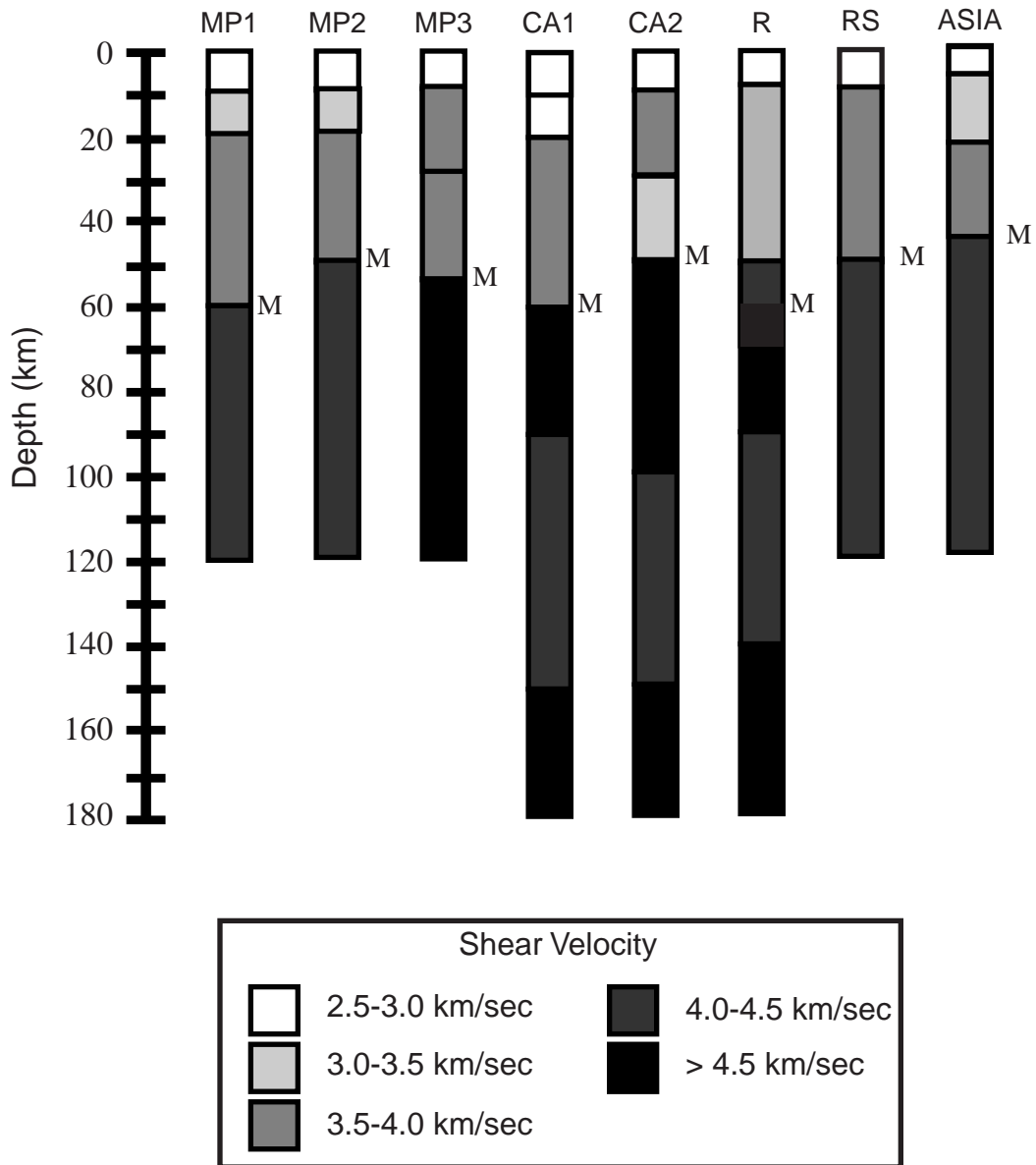


Figure 4.1.1. Models from previous studies: MP1 = Mahdi and Pavlis (1998) eastern Tien Shan path; MP2 = Mahdi and Pavlis Tarim-Tien Shan path; MP3 = Mahdi and Pavlis Turan Tien Shan path; CA1 = Cotton and Avouac (1994) central Tien Shan path; CA2 = Cotton and Avouac eastern Tien Shan path; R = Romanowicz (1982) Tibet path (from phase velocities); RS = Roecker et al. (1993) central Tien Shan; ASIA = Kosarov et al. (1993) and Patton (1998); M = Moho depth.

If travel time residuals are correlated with the age of the latest episode of thermal upheaval in the upper mantle then the eastern Tien Shan should be a region with a “hot” upper mantle and the western Tien Shan should be a region with a “cold” upper mantle (Vinnik and Saipbetkova, 1984). Vinnik and Saipbetkova (1984) concluded that the differences in the travel-time residuals (and hence mantle thermal properties) are best described by using the combined effects of differences in crustal thickness and the lateral movement of crustal rocks by the Tianshan-Fergana (Figure 2.2.2) fault as a thermal boundary.

Three-dimensional (3-D) studies of central Asia also examined velocity variations in the crust and upper mantle. Using arrival times of P and S waves from regional and teleseismic earthquakes and explosions recorded over 30 years, Roecker et al. (1993) mapped seismic velocity variations beneath the Tien Shan. The results indicate that the seismic velocities increase monotonically with depth. The fit to the observations in the model increased by at least 30%. The one-dimensional models are then used as an initial model for the tomographic investigation. Resolution was adequate into the deepest layers (300-400 km). Results show velocities at midcrustal depths at about 6.4 km/sec and upper mantle velocities at 8.0 km/sec (Roecker et al., 1993). Velocities in this region imply the existence of a positive buoyancy force that may be uplifting the mountains because no evidence for a lithospheric root is found (Roecker et al., 1993).

Ghose et al. (1998) also examined P and S wave velocity variations beneath the Tien Shan using arrival times from earthquakes and quarry blasts (Figure 3.1.1). Models obtained by shooting rays from the sources to the receivers. Spike and checkerboard synthetic tests show the resolution of their three-dimensional model can fully recover an anomaly to a depth of 27 km for P and S waves.

The P and S models show increased heterogeneity at shallow depths (< 7 km). A strong midcrustal low velocity zone was imaged beneath the western Tien Shan which correlates with high-conductivity zones of fluid migration along active faults and may imply a crustal decoupling zone at the brittle-ductile transition (Ghose et al., 1998). Along the mountain front, crustal shortening is shown by relatively steep south-dipping reverse faults that mark the boundary between the Kazakh Platform and the Tien Shan. This is consistent with the seismicity, seismic velocity gradients, and earthquake source mechanisms.

4.2 Receiver Function Analysis of Central Asia

Another technique to determine variations in crustal thickness is by using receiver functions. Receiver functions are a time series calculated from teleseismic P wavetrains that can be interpreted in terms of the reflections and transmissions of mode-converted waves at discrete boundaries beneath the recording station (Bump and Sheehan, 1998). Bump and Sheehan (1998) examined 42 teleseismic P waveforms from the Tien Shan recorded at distances between 30° and 90° with body wave magnitudes greater than 6.0 and recorded with good signal-to-noise ratios. A single layer approximation with a P-to-S conversion at the base of the crust was used to find the gross crustal variations across the Tien Shan (Bump and Sheehan, 1998). Their results show crustal thickness that average 42 km beneath the Kazakh Shield increasing to about 60 km beneath the Tien Shan. Their model is in good agreement with gravity measurements and a simple model of crustal shortening that can be explained by an Airy lithospheric root (Burov et al., 1990; Bump and Sheehan, 1998).

Kosarov et al. (1993) also used teleseismic receiver functions to estimate the crustal structure beneath the Tien Shan. They inferred that the upper mantle beneath the Tien Shan is hot. Upwelling of hot mantle material could account for the lower than normal velocities (3.0-3.4 km/sec) between 20 and 40 km as opposed to 3.5-4.0 km/sec which is expected at these depths. A hot mantle model can explain low velocities observed in the upper mantle and high attenuation of high frequency teleseismic waves. A low-density, hot mantle suggests that positive buoyancy forces contribute to the mountain building process, in addition to the horizontal crustal shortening caused by the collision of India into Eurasia.

The numerous crustal studies of central Asia provide a better picture of the dynamic processes taking place in central Asia. It is accepted that central Asia is a region with a crust thicker than global averages. In Figure 4.1.1, I compare previous models of crustal structure in central Asia (the location of studies in Figure 3.1.1). There are still questions on how this thickened crust maintains its isostatic equilibrium. Previous studies suggest that there is probably a hot mantle that plays a significant role in central Asia deformation. In general, the crust thickens north to the Tien Shan and south to the Tibetan Plateau. Shear-wave velocities increase with depth; however,

Ghose et al. (1998) found a low-velocity zone in the crust that may be related to upwelling. However, more work is needed to fully explain the processes taking place in central Asia.

CHAPTER 5 SURFACE-WAVE DISPERSION ANALYSIS

5.1 Earthquakes and Stations

Data are collected for this study from 14 broadband seismometers located throughout Asia (Figure 1.1.1; Table 1). Twenty-six regional earthquakes recorded from 1987-1996 with surface-wave magnitudes from 4.8 to 6.2 and are chosen based on the availability of moment tensor solutions and reliable depth estimates from previous studies, relative location to the Lop Nor nuclear test site, and adequate signal-to-noise ratios (Table 2). Station locations are shown in Figures 1.1.1 and 1.1.2. Earthquakes are concentrated in the western portion of the study area roughly parallel to the Tien Shan Mountains. The remaining events are located north of the Junggar Basin and in the south near Lop Nor nuclear test site (Figures 1.1.1 and 1.1.2).

5.2 Surface Waves

Large earthquakes excite surface waves that appear as the highest amplitude waves on a broadband seismogram recorded more than a few 100 km from the source. Surface waves result from different body-wave phases interacting at the free surface. Incident P and SV waves interact at the free surface causing interference and creating a wave that travels along the surface as a Rayleigh wave. Rayleigh particle motion for the is retrograde elliptical in the direction of propagation to a depth $L/5$ (L is the wavelength of the Rayleigh wave) where it goes to zero. Below this depth, elliptical particle motion becomes prograde. A Rayleigh wave is found in the vertical plane with no tangential motion. Love waves are the second type of surface wave and result from SH waves trapped near the surface when the velocity structure turns the energy toward the surface. The SH component of the S wave has displacements parallel to the surface and can only have total reflections from the free surface (e.g. Lay and Wallace, 1995). A waveguide is produced when a ray strikes a reflecting horizon at post critical angles, then all the energy is trapped within the waveguide (e.g. Lay and Wallace, 1995). Love waves travel faster than Rayleigh and appear on the transverse component of the seismogram. For a review of theoretical background of surface waves see Aki and Richards (1980) and Lay and Wallace (1995). Dispersion is the apparent surface-wave velocity that depends on the period and reflects the velocity variation with depth. Dispersion appears on a seismogram as different periods arriving at different times. In general, short

Table 1 List of Stations Used in the Study

Latitude (°N)	Longitude (°E)	Elevation (meters)	Station ID
42.64	74.49	1645	AAK
40.02	116.17	137	BJI
53.06	70.28	330	BRV
18.79	98.98	316	CHTO
49.27	119.74	595	HIA
25.12	102.74	1945	KMI
50.71	78.62	184	KUR
29.70	91.15	3774	LSA
36.08	103.84	1560	LZH
46.81	81.98	600	MAK
33.65	73.25	629	NIL
43.23	77.22	1120	TLG
51.68	103.64	579	TLY
43.82	87.69	903	WMQ

Table 2 List of Events Used in the Study

No.	Date	Origin Time UT	Latitude (°N)	Longitude (°E)	Depth km	Magnitude M_S
1	Jan. 5, 1987	22:52	42.00	81.32	20.0	5.9
2	Jan. 24 1987	08:09	41.52	79.29	5.0	6.0
3	Feb. 25, 1987	19:56	38.03	91.14	25.0	5.7
4	March 3, 1987	09:41	41.36	79.28	40.0	5.1
5	Sep. 18, 1987	21:58	47.28	89.67	30.0	5.3
6	Dec. 22, 1987	00:16	41.36	89.66	20.0	5.9
7	June 17, 1988	13:30	42.94	77.50	30.0	5.3
8	July 23, 1988	07:38	48.72	90.51	20.0	5.5
9	Dec. 15, 1988	06:40	46.55	95.49	20.0	5.3
10	June 14, 1990	12:47	47.89	85.12	25.0	6.2
11	Aug. 3, 1990	09:15	47.95	84.96	35.0	6.1
12	Oct. 24, 1990	23:38	44.10	83.88	35.0	5.4
13	Nov. 12, 1990	12:28	42.94	78.08	5.0	5.9
14	Dec 1, 1990	18:09	40.80	73.62	20.0	5.0
15	Feb. 25, 1991	14:30	40.33	78.95	5.0	5.5
16	Aug 19, 1991	06:05	46.95	85.33	35.0	5.7
17	Dec. 24, 1992	05:09	42.18	72.20	1.0	5.2
18	Oct. 2, 1993	08:42	38.14	88.64	15.0	6.2
19	Dec. 30, 1993	14:24	44.72	78.79	25.0	5.8
20	May 5, 1994	09:14	40.28	78.87	35.0	4.8
21	Aug. 8, 1994	14:18	40.23	78.68	25.0	4.8
22	Sep. 9, 1995	04:39	41.81	81.59	10.0	5.3
23	Nov. 1, 1995	12:29	42.99	80.31	15.0	5.5
24	Jan 18, 1996	09:33	41.83	77.48	25.0	5.2
25	March 12, 1996	18:43	48.44	88.14	15.0	5.6
26	March 19, 1996	15:00	39.99	76.70	10.0	5.7

period surface waves, which sample rocks closer to the surface, travel slower than long period waves. Long period waves are sensitive to faster velocities found deeper in the Earth. Both Rayleigh and Love waves exhibit dispersion and are used to estimate shear-velocity variations in the crust and upper mantle.

Seismic sources usually excite a continuous spectrum of surface-wave periods. Each harmonic component has a velocity, $c(\omega)$, called a phase velocity where $\omega = 2\pi f$ (radian frequency) that depends on the medium parameters (layer thickness, P and/or S velocities, etc.). Wave disturbances with a wide spectrum of periods interfere with each other producing constructive and destructive patterns. Constructive patterns travel along the surface as wave packets with well-defined group velocities, $U(\omega)$, that depend on the medium parameters and the variation in phase velocity with frequency. Group velocity curves often have a local minimum at 20 and 200 seconds

period known as an Airy phase and results from a large amount of energy arriving at the same time.

5.3 Group Velocity Measurement

Measuring group and phase velocities involves several steps that require information obtained from seismograms. First, the quality of the earthquake data must be checked to insure a reasonable signal-to-noise ratio of the seismogram. Background “noise” may be other energy (e.g. body waves) that arrives at the same time as the surface wave. Next, the instrument response must be removed from the seismogram by deconvolution. In SAC, four frequency values define a cosine window applied to the instrument deconvolution to reduce long and short-period noise amplified by spectral division (Tapley and Tull, 1992).

Once displacements are computed a multiple-filter analysis (Dziewonski et al., 1969; Herrmann, 1973; implemented by Ammon, 1998) is performed to estimate group velocities for the 26 events. A Gaussian filter with peak amplitude centered at the desired period is applied to the seismogram in the frequency domain. The peak of the envelope of the corresponding time domain signal is used to estimate the group travel time. The time of the peak is estimated by fitting a quadratic curve to the largest three values (allowing interpolation between time samples). In practice, the true period represented in the filtered signal may not correspond to the Gaussian filter's center period. To account for possible bias produced by changing spectral amplitudes, an instantaneous period is measured at the time of the envelope peak. The group velocity for a given period is estimated by dividing the distance between the station and source by the group arrival time. The process is repeated for each period in a specific range and is plotted versus group velocity.

Once group velocities have been estimated, a mode isolation filter (Herrin and Goforth, 1977) can be constructed and applied to the signal to isolate the fundamental mode from the signal-generated and ambient Earth noise. Mode-isolation provides smooth, stable spectral amplitudes and eases estimation of signal phase. This procedure is illustrated in Figure 5.3.1 and 5.3.2. Figure 5.3.1 is a plot of an observed vertical component seismogram, its corresponding rotated seismogram, and the mode-isolated surface-wave seismogram used to calculate the phase velocities. Fig-

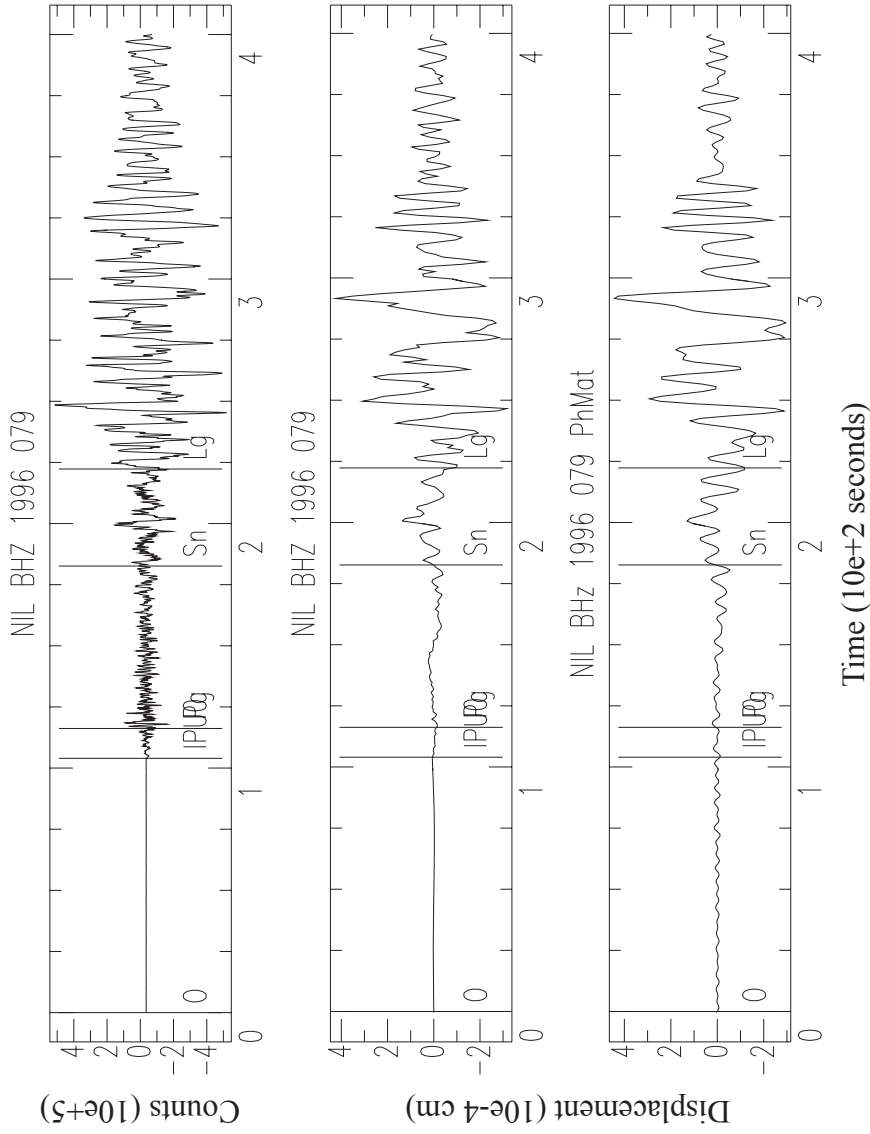


Figure 5.3.1. Vertical component seismogram from the March 19, 1996 event at station Nilore, Pakistan. The top panel is the raw data seismogram, the middle panels show the rotated seismogram, and the bottom is the phase matched-filtered seismogram from the program SWMFA.

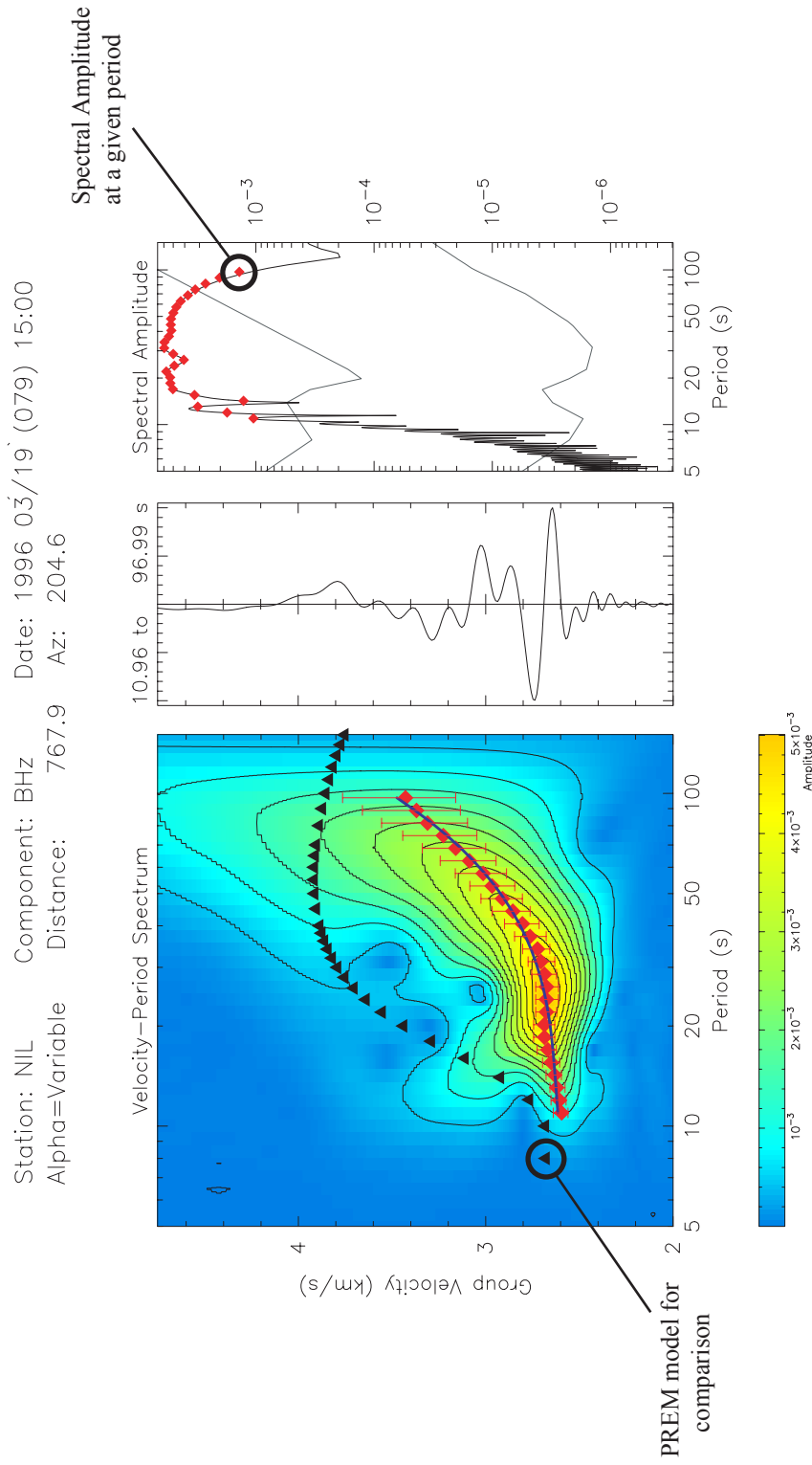


Figure 5.3.2. Output from SWMFA, including spline-fit dispersion curve, velocity amplitude, and spectral amplitude (left to right, respectively).

ure 5.3.2 is the output of the program Surface Wave Multiple Filter Analysis (SWMFA), showing the estimated group velocity, group velocity as a function of period, and the spectral amplitude.

Dispersion data from this study included only the vertical (Rayleigh) and transverse (Love) component seismograms. Criteria for periods selected for the group velocity dispersion curves include: keeping as many periods as possible, but only those with adequate signal strength and selecting periods that lie along the smoothest part of the spectral amplitude curve. The average for all the Love-wave data is shown in Figure 5.3.3 and the Rayleigh in Figure 5.3.4.

For analysis, group velocity observations from the 26 events were averaged for three paths (discussed in section 5.5) and include periods from 8 to 100 seconds. Observed group velocities range from 2.8 to 3.5 km/sec and show a pronounced Airy phase that arrives with about 20 seconds period. Observations show Tarim and Junggar Basin paths ~0.6 km/sec slower than paths through the Tien Shan. Implications of path dependence are discussed in chapter 6.

5.4 Phase-Velocity Measurement

Phase velocities for the 26 events in this study are estimated using the single-station method and assuming source phase corrections from available moment-tensor and depth estimates. The observed phase of a seismic surface wave can be expressed as an initial phase from the source acted upon by a set of linear filters. Source phase, $\phi_s(\omega)$, and observed phase, $\phi_0(\omega)$, are related by

$$\phi_0(\omega) = \phi_s(\omega) + \phi_p(\omega) + \phi_i(\omega) \quad (5.4.1)$$

where $\omega = 2\pi f$ (radian frequency), $\phi_i(\omega)$ is the instrument phase, and $\phi_p(\omega)$ is the propagation phase. To estimate the phase velocity, the initial phase at the source, the origin time, and the distance traveled must all be known. To calculate the initial phase, the faulting mechanism and source depth must be known. The instrument response is known and already removed when the seismogram is deconvolved to recover ground displacement. Constrained moment-tensor solutions provide good source correction estimates and were computed from moment tensors of the 26

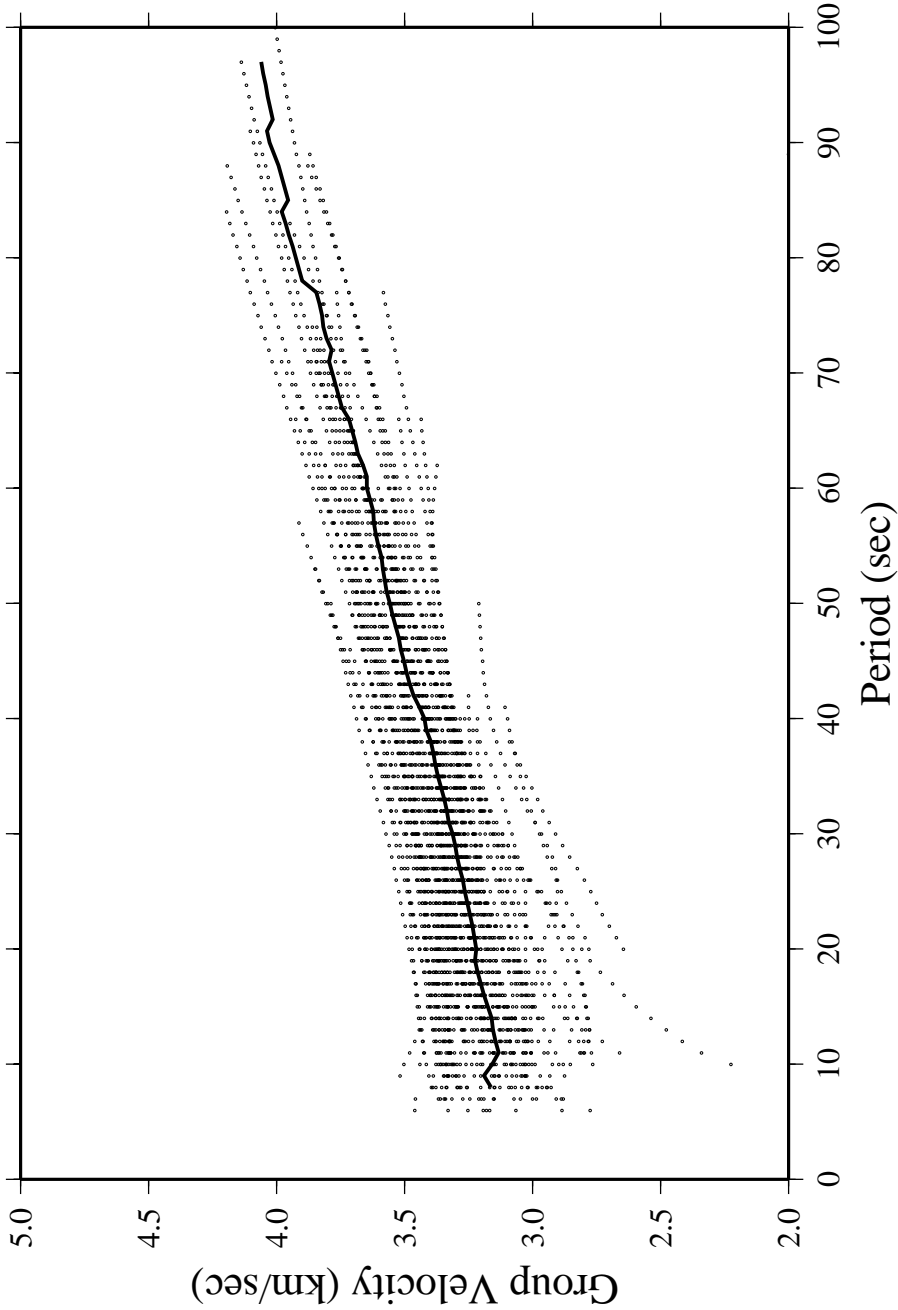


Figure 5.3.3. Observed (dots) and average (solid line) Love-wave group velocities. Dots are the observed Love-wave group velocities at each period. Solid line is the calculated mean for all 26 events.

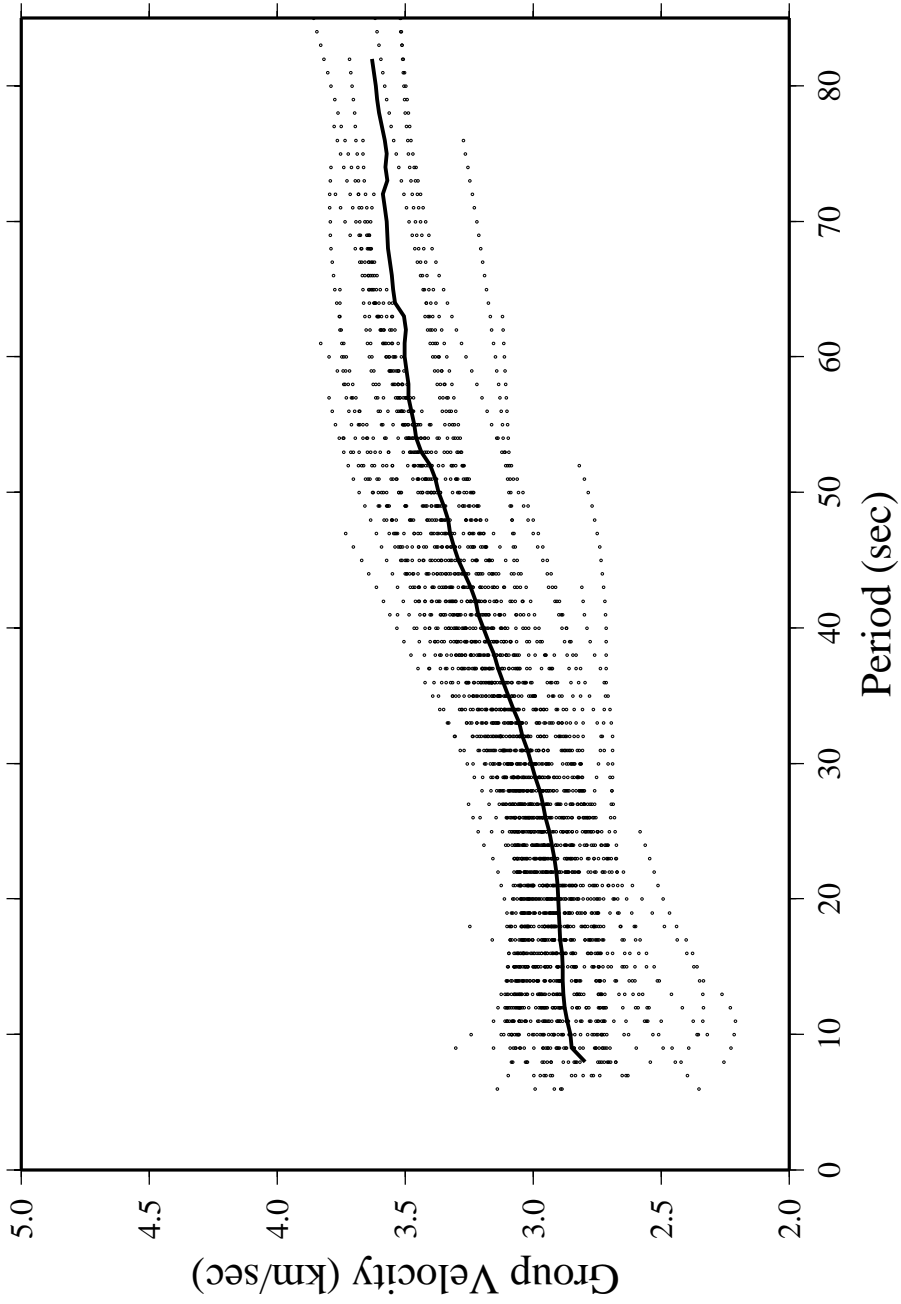


Figure 5.3.4. Observed (dots) and average (solid line) Rayleigh-wave group velocities. Dots are the observed Rayleigh-wave group velocities at each period. Solid line is the calculated mean for all 26 events.

events using the method of Patton (1982). The propagation phase term depends on the phase velocity of the structure. The expression for the source and instrument corrected phase term is

$$\phi_p(\omega) = \frac{\omega r}{c(\omega)} \quad (5.4.2)$$

where $\omega = 2\pi f$ (radian frequency, r = source-receiver distance, and $c(\omega)$ = phase velocity. Solving for the phase velocity, $c(\omega)$, introduces a $2\pi N$ uncertainty without changing the observed waveform. The $2\pi N$ term (N is an integer) represents the periodicity of the harmonic term in the phase velocities and is estimated using long-period observations, which should converge to globally averaged values at long-periods (i.e. estimated phase velocities are compared to reference velocities to determine the correct branch of the dispersion curve) as shown in Figure 5.4.1. The average phase velocities for all the Love-wave dispersion estimates are shown in Figure 5.4.2 and Rayleigh-wave estimates in Figure 5.4.3.

Observed phase velocities range between 2.8 and 4.0 km/sec and like the group velocities, phase velocities show considerable path dependence. In general, paths crossing the Tarim and Junggar Basins are ~ 0.5 km/sec slower than those paths crossing the Tien Shan. These observations are consistent with previous studies and expected geologic path dependence (Patton, 1982; Romanowicz, 1982; Pavlis and Mahdi, 1996; Mahdi and Pavlis, 1998).

5.5 Path Averaging

Phase velocity dispersion curves obtained were averaged to minimize the errors due to noise found in any particular path. Events recorded at Urumqi (WMQ) were divided into three clusters and averaged along three paths. (Figure 5.5.1). The first cluster includes eight events located mostly in the Tien Shan with a few located along the edge of the Tarim Basin. Collectively, the observed dispersion velocities for these events comprise data for the "Tarim-Tien Shan" path. The cluster to the north of WMQ in the Junggar Basin and Altay Mountains includes three events and is referred to as the Junggar path. The final three events are located to the south of WMQ and are referred to as the Tibet-Tarim path.

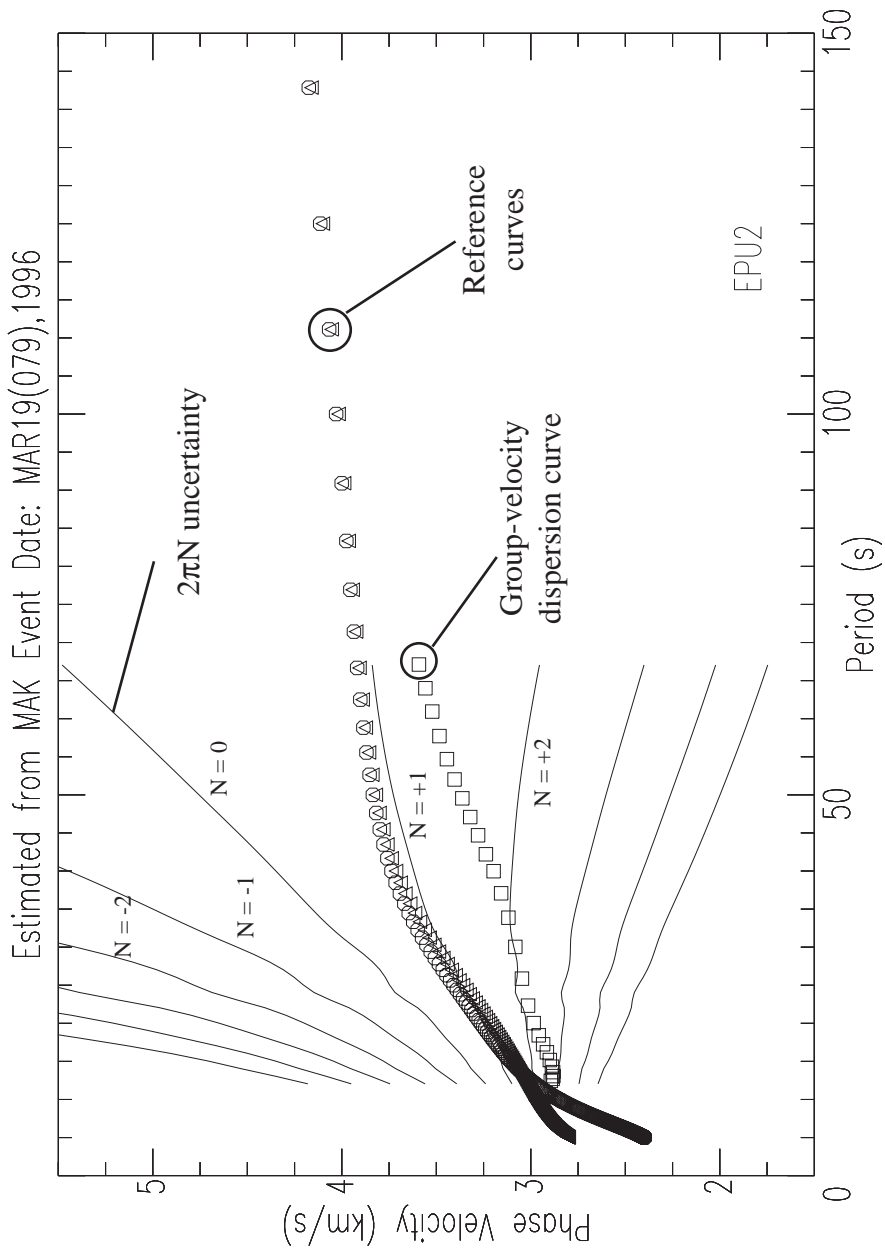


Figure 5.4.1. Phase velocity output from the March 19, 1996 earthquake recorded at MAK. Circles and triangles indicate reference velocity dispersion curves. Squares indicate estimated group velocity curve. Lines spreading out are the $2\pi N$ uncertainties introduced into the phase calculation. The correct branch of $2\pi N$ is chosen ($N = +1$) on how it fits the reference curves.

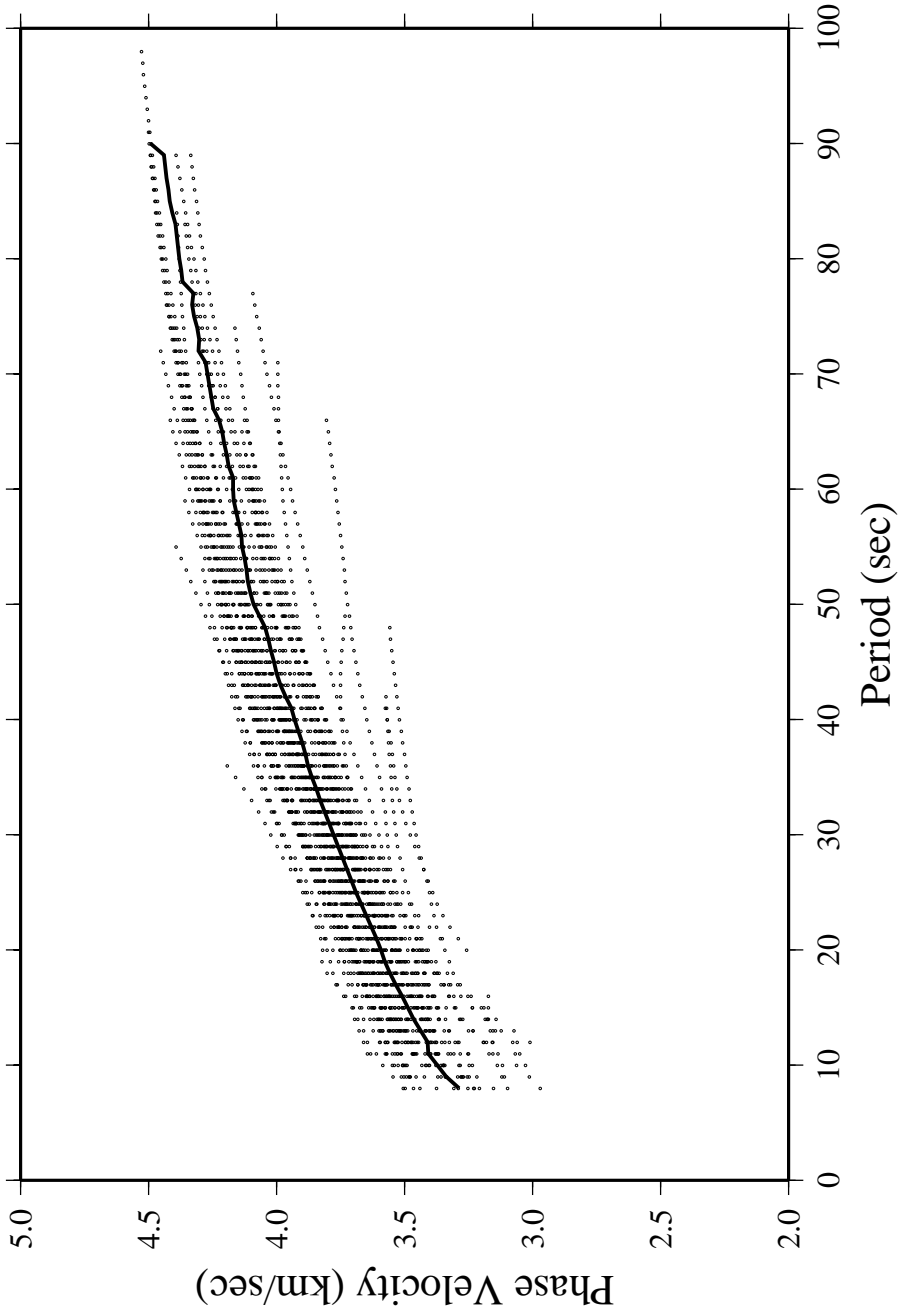


Figure 5.4.2. Observed (dots) and average (solid line) Love-wave phase velocities. Dots are the observed Love-wave phase velocities at each period. Solid line is the calculated mean for all 26 events.

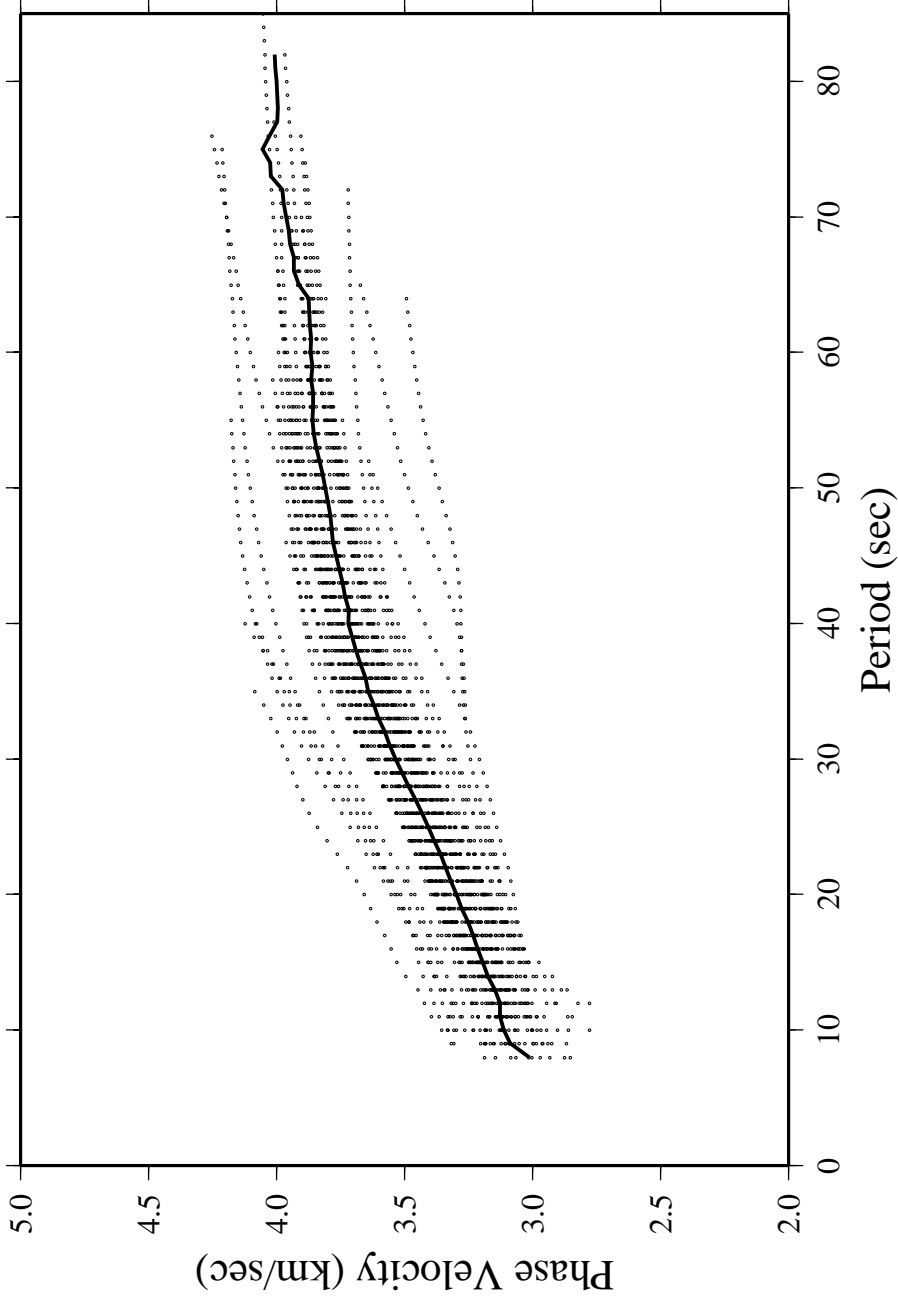


Figure 5.4.3. Observed (dots) and average (solid line) Rayleigh-wave phase- velocities. Dots are the observed Rayleigh-wave phase velocities at each period. Solid line is the calculated mean for all 26 events

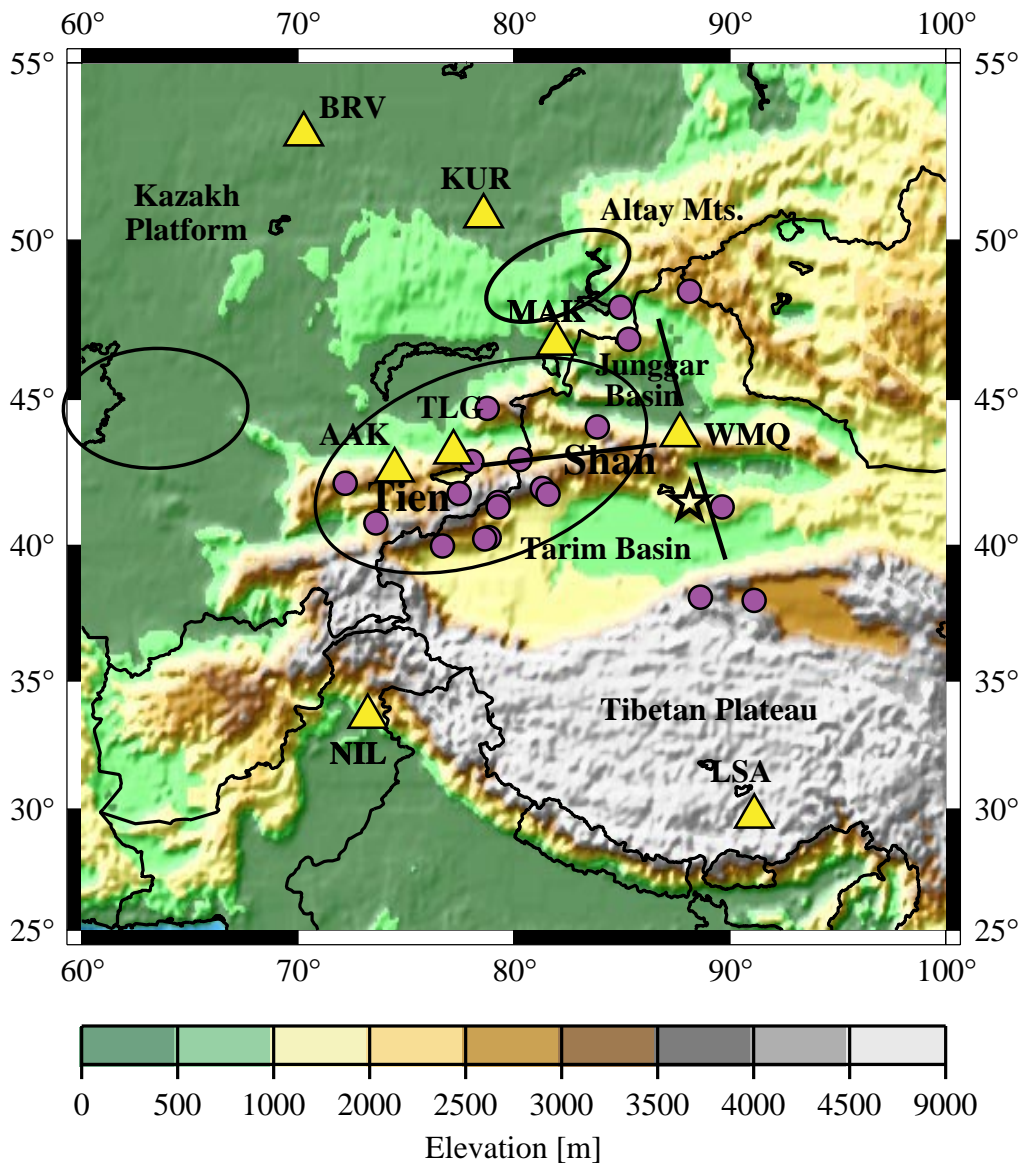


Figure 5.5.1. Region map showing locations of average phase velocity paths used in the inversions. See figure 1.1.1 for explanation of map symbols.

For the phase and group velocity dispersion observations, the mean, median and standard deviation at each period were calculated for each path. Figures 5.5.2-5.5.5 show the average group and phase velocity dispersion curves for the Junggar Basin path. The Love-wave group velocities show large standard deviations at the short periods and reflect noise in the data and possible scattering of the waves. The group velocity curve shows the characteristic Airy phase arriving at around 20 seconds period. The average path represents energy traveling through the Junggar Basin and is about 0.5 km/sec slower than a path crossing mountains.

Average group and phase velocity dispersion curves for the Tibet-Tarim Path are shown in 5.5.6-5.5.9. Rayleigh group velocities show large standard deviation at the long periods and reflects scatter of the data. There are only three events for this path and there is significant scattering at the long periods. An Airy phase is not pronounced in the group velocities. Lack of data for the path makes results for this path very suspect. A large amount of structural heterogeneity is represented by this path.

Dispersion curve average results for the Tarim-Tien Shan path are shown in figures 5.5.10-5.5.11. Only the Rayleigh-wave group velocity shows a slight Airy phase around 20 seconds period. Errors in the Rayleigh-wave phase velocities result from noise in the data and possible ray scattering because of paths crossing the Tarim Basin and Tien Shan. Discontinuities in the group and phase velocity curves result from scattering in the data. The lack of standard deviation bars at the long-periods results from only one seismic record being evaluated.

5.6 Sources of Uncertainty

Since estimating surface wave dispersion requires some important assumptions, potential sources of uncertainty must be evaluated to insure meaningful results during the shear velocity inversion process. Noise, scattering, and errors in earthquake origin times can decrease the accuracy of the shear velocity and depth found during an inversion (Der et al., 1970).

Tests were performed to show how changing the epicenter of an earthquake can affect the phase velocity. The term for the corrected phase velocity in equation (3.4.2) is dependent on r . To test

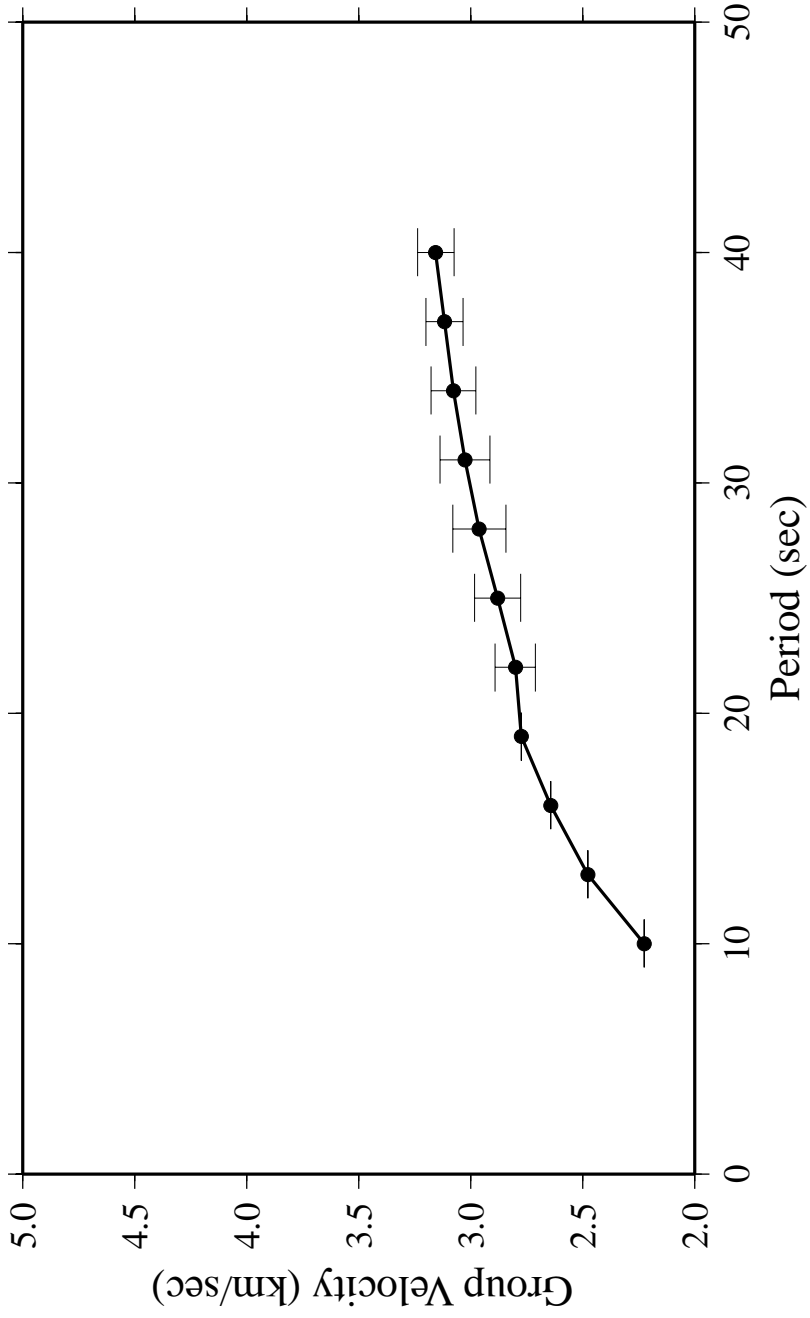


Figure 5.5.2. Observed Love-wave group-velocities with calculated standard deviations for the Junggar path.

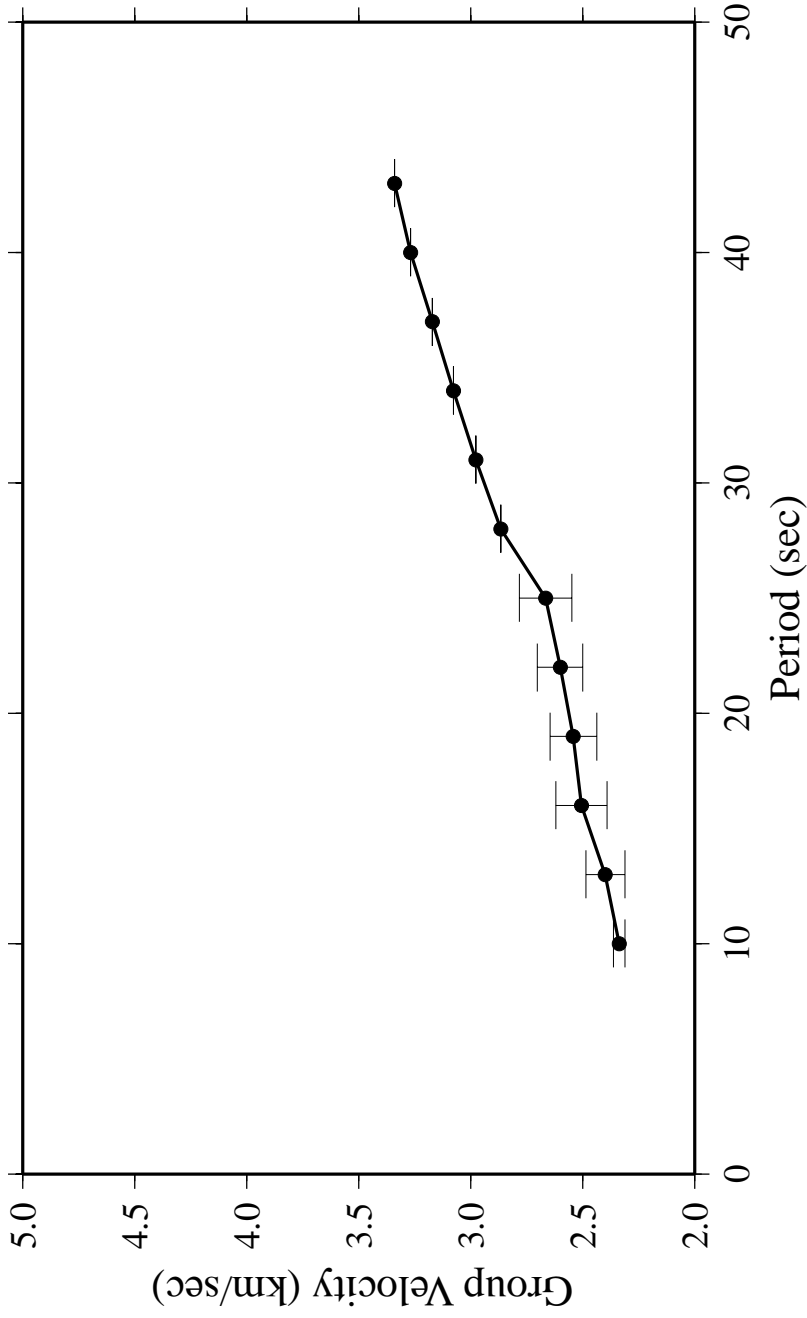


Figure 5.5.3. Observed Rayleigh-wave group-velocities with calculated standard deviations for the Junggar path.

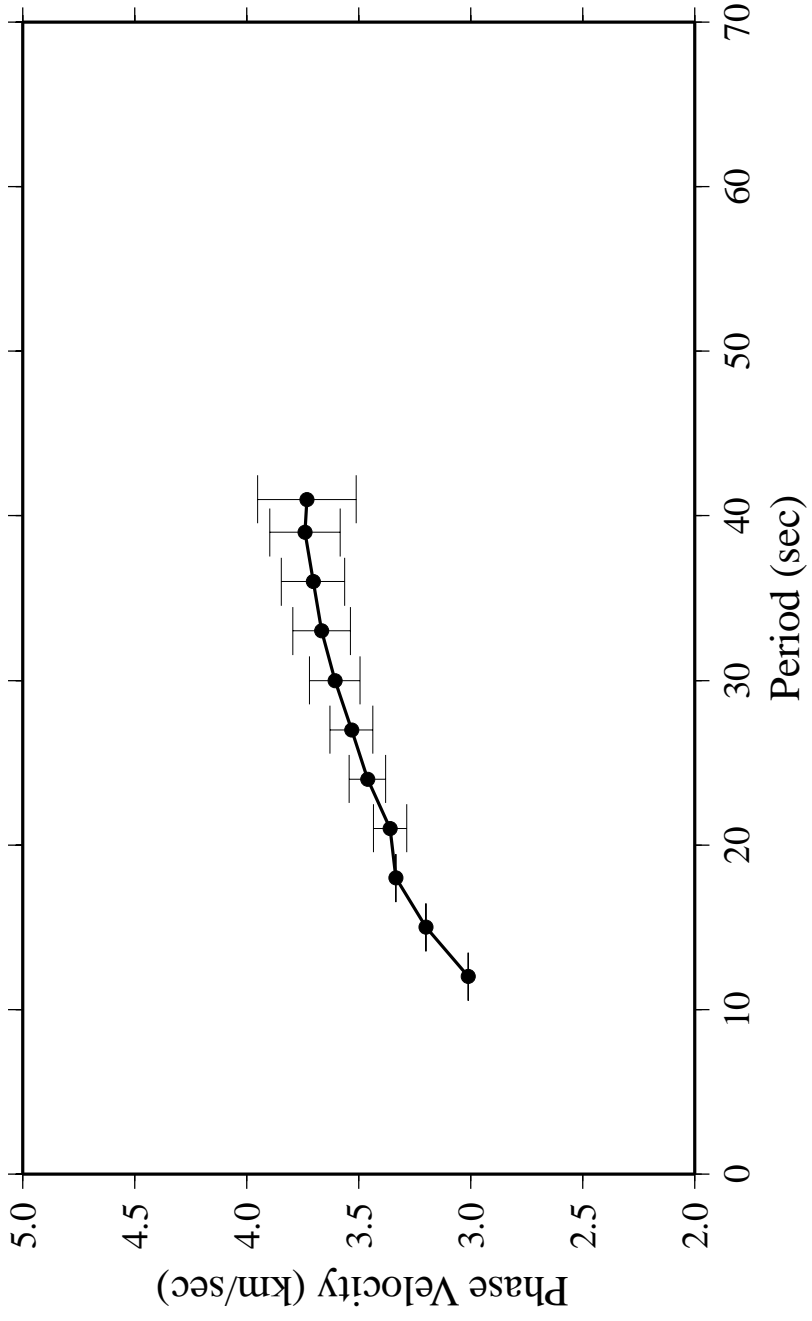


Figure 5.5.4. Observed Love-wave phase-velocities with calculated standard deviations for the Junggar path.

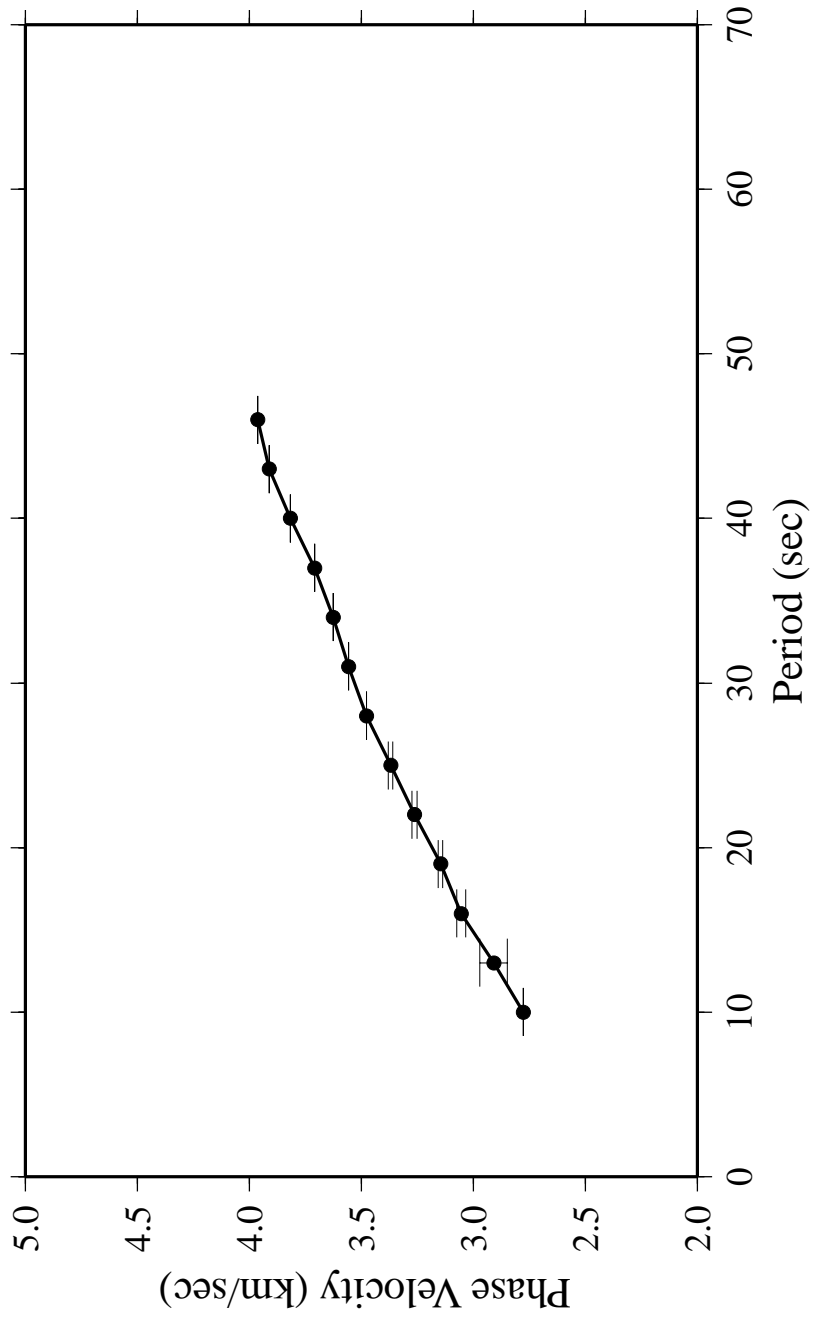


Figure 5.5.5. Observed Rayleigh-wave phase-velocities with calculated standard deviations for the Junggar path.

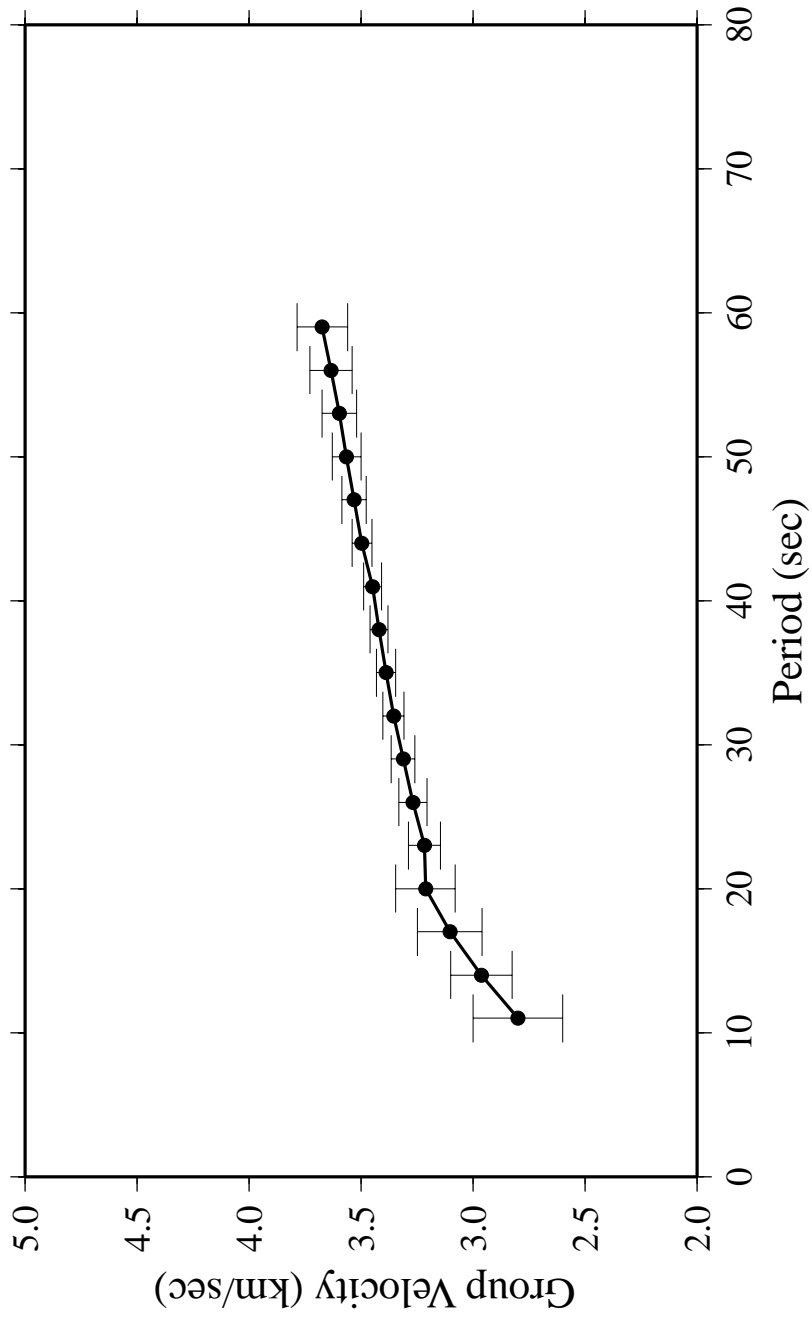


Figure 5.5.6. Observed Love-wave group-velocities with calculated standard deviations for the Tibet-Tarim path.

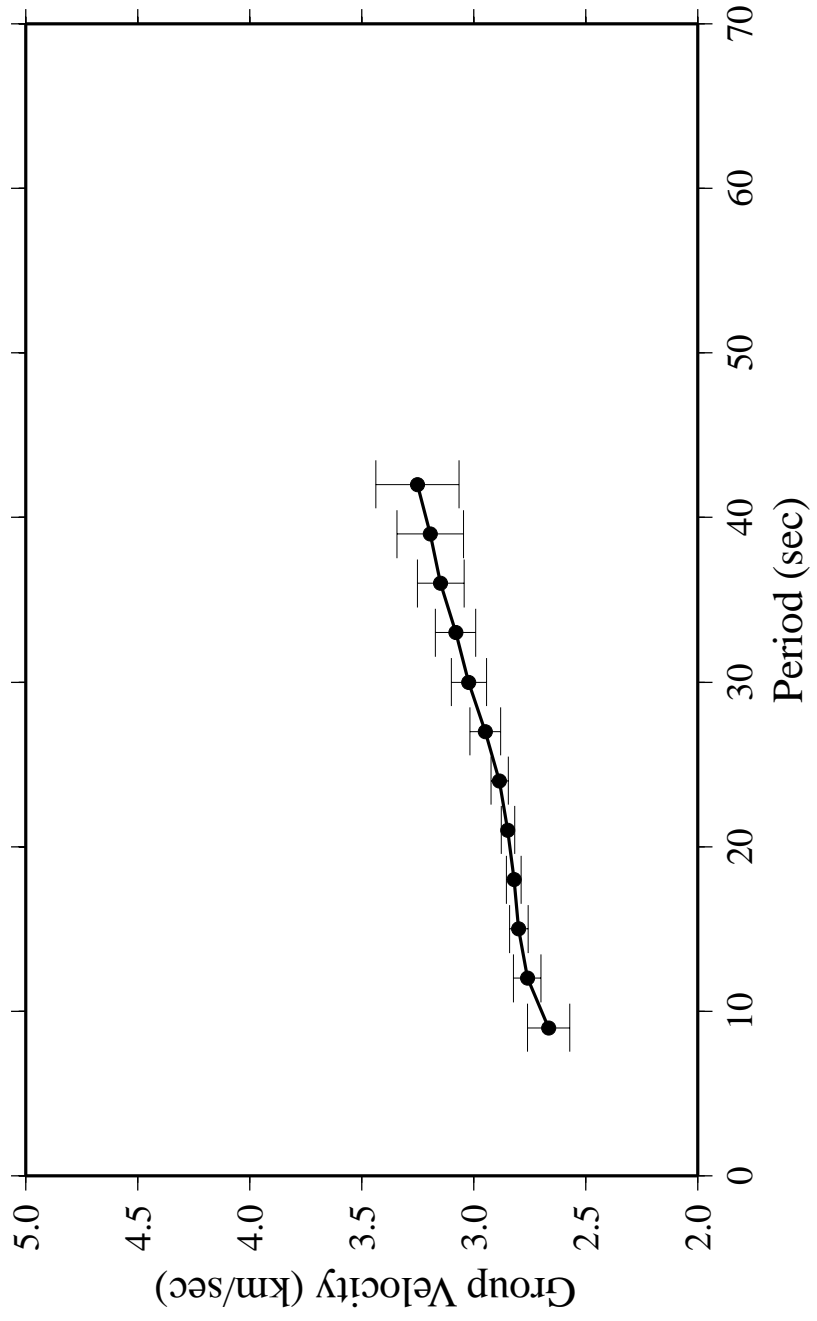


Figure 5.5.7. Observed Rayleigh-wave group-velocities with calculated standard deviations for the Tibet-Tarim path.

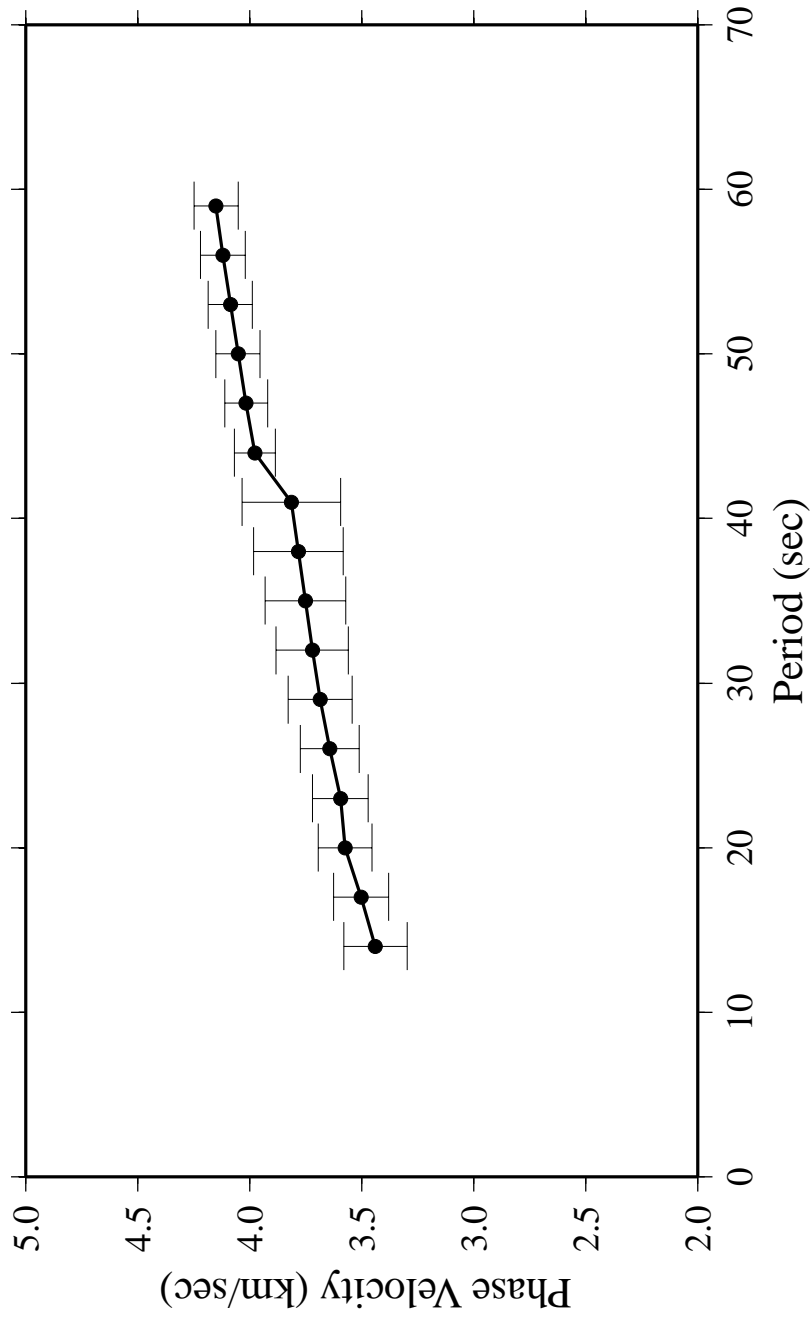


Figure 5.5.8. Observed Love-wave phase-velocities with calculated standard deviations for the Tibet-Tarim path.

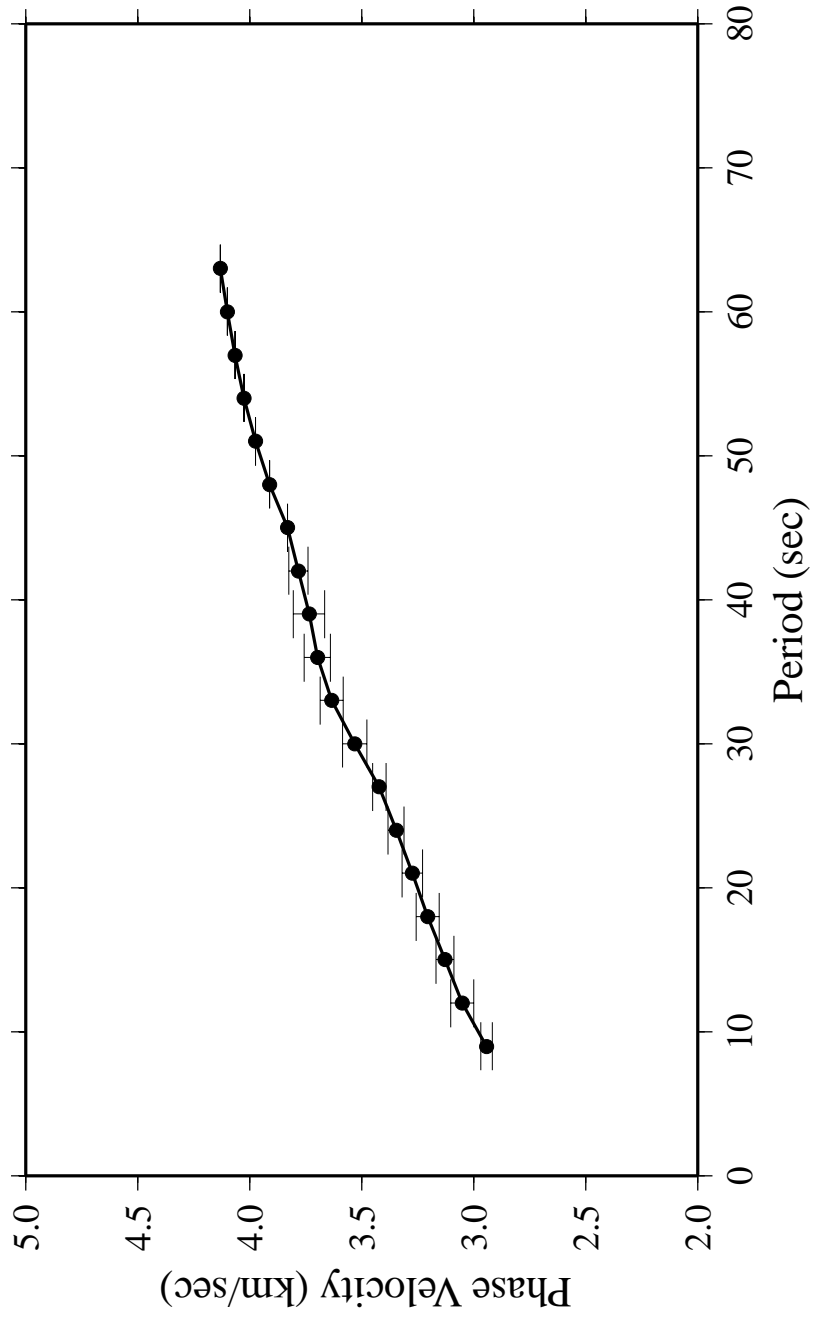


Figure 5.5.9. Observed Rayleigh-wave phase-velocities with calculated standard deviations for the Tibet-Tarim path.

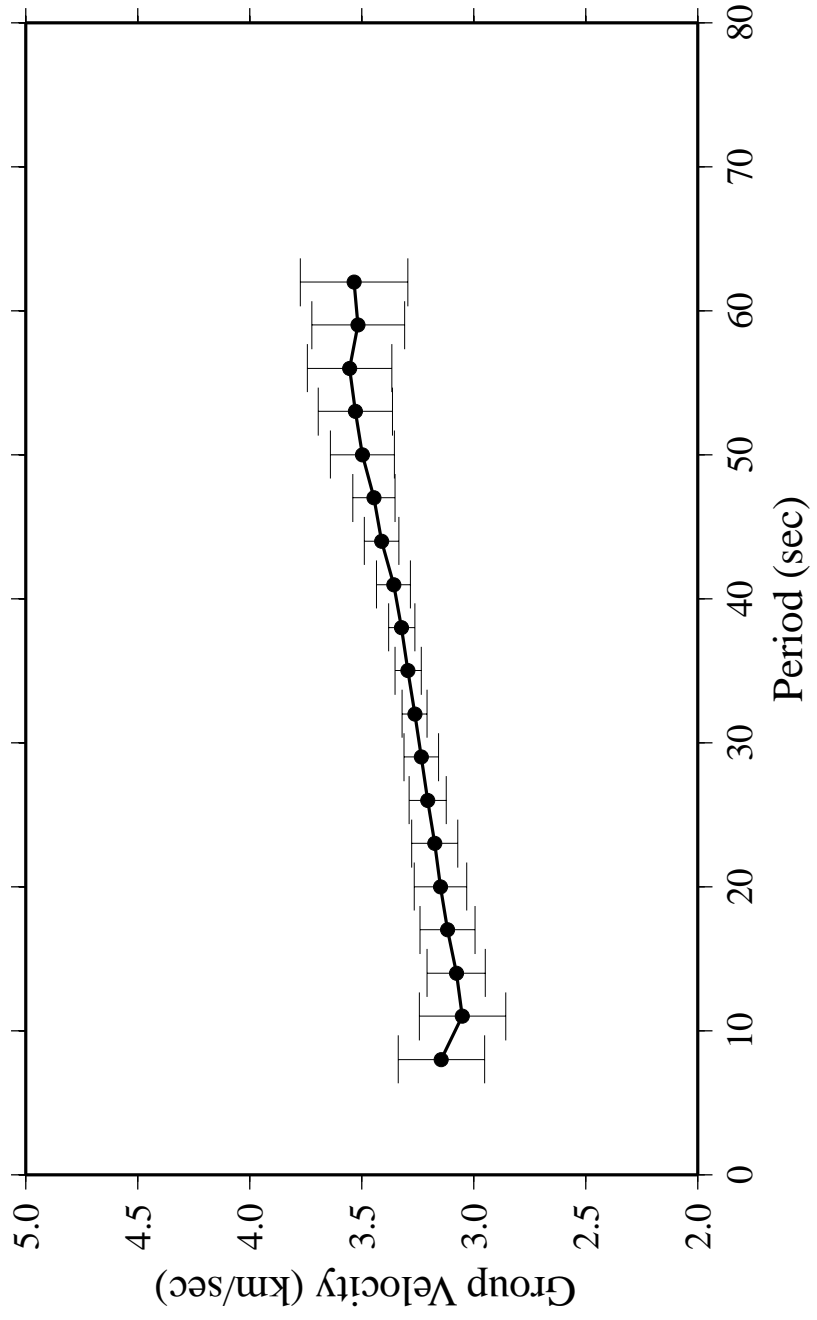


Figure 5.5.10. Observed Love-wave group-velocities with calculated standard deviations for the Tarim-Tien Shan path.

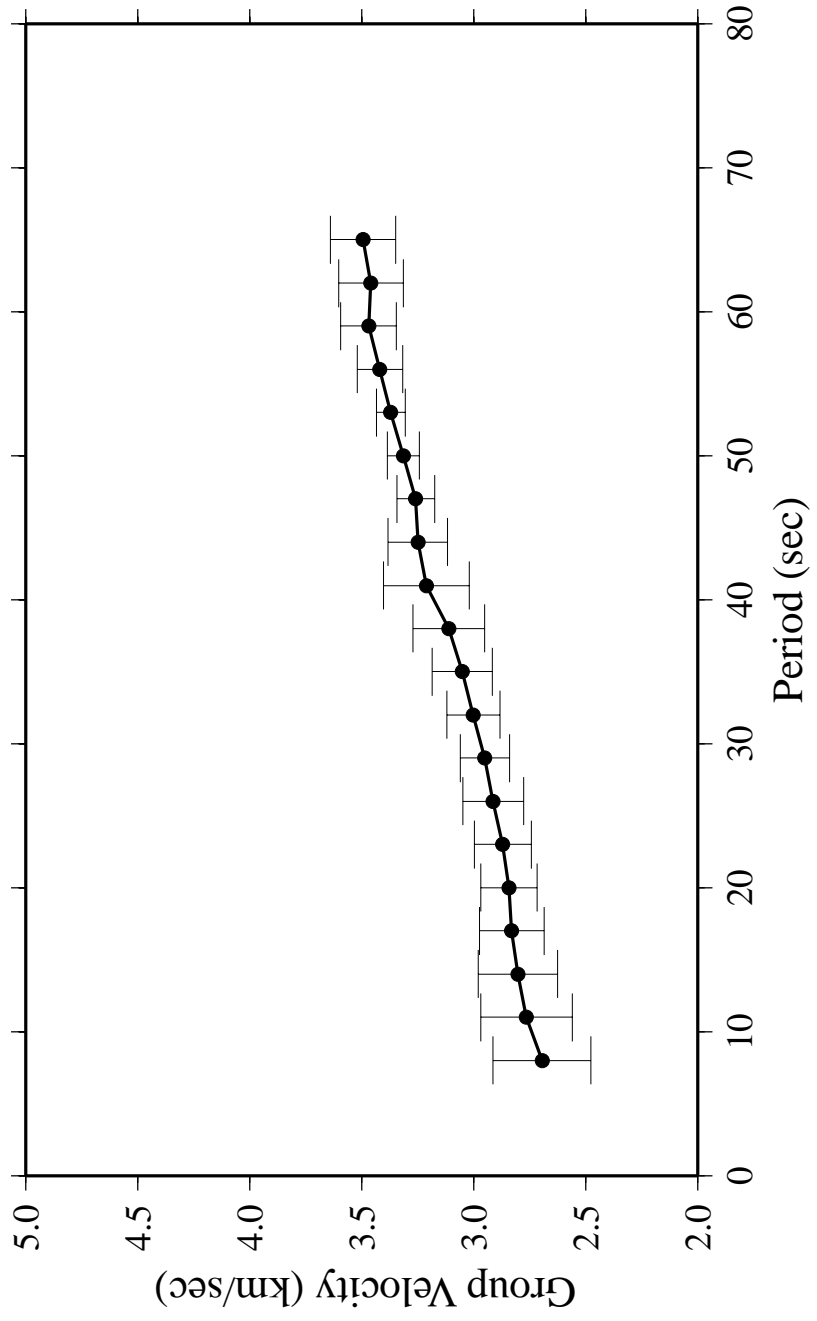


Figure 5.5.11. Observed Rayleigh-wave group-velocities with calculated standard deviations for the Tarim-Tien Shan path

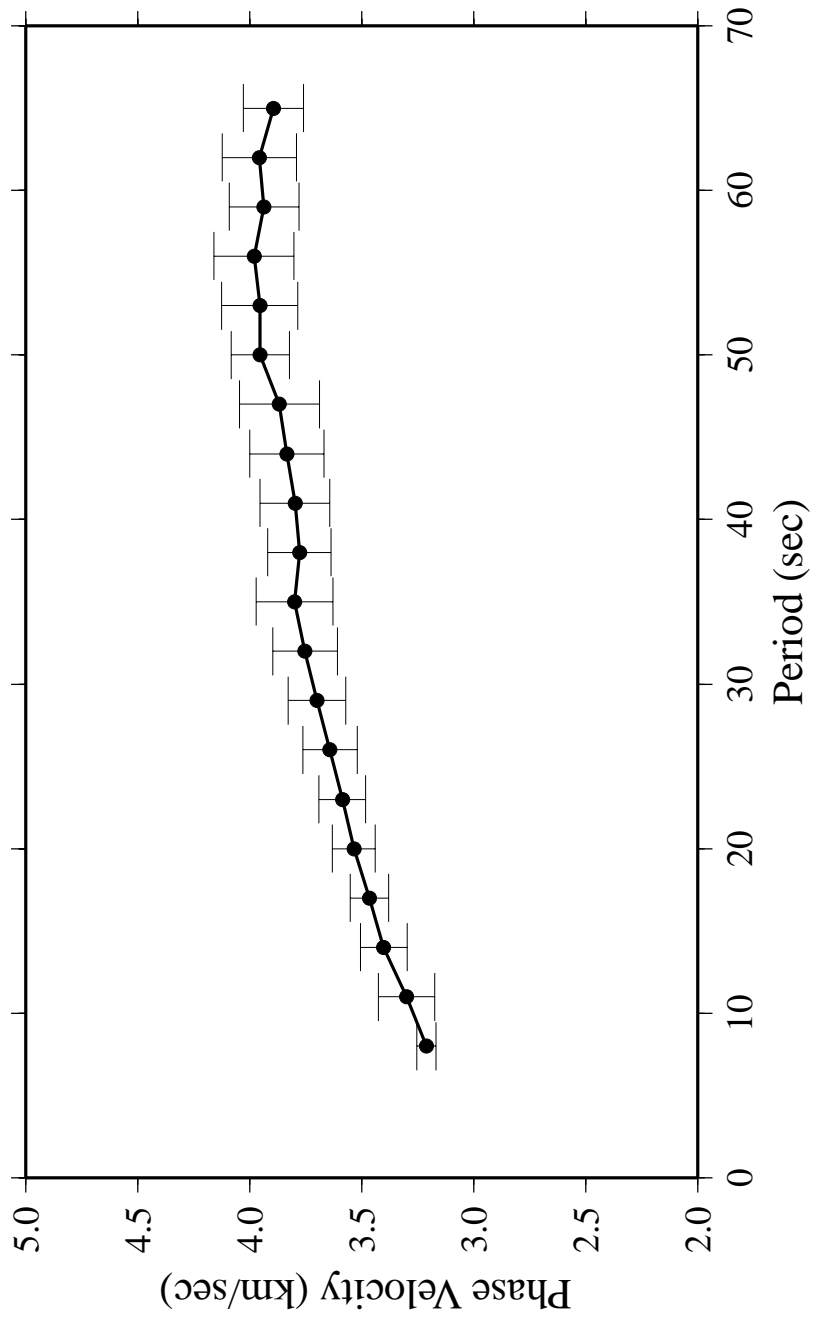


Figure 5.5.12. Observed Love-wave phase-velocities with calculated standard deviations for the Tarim-Tien Shan path

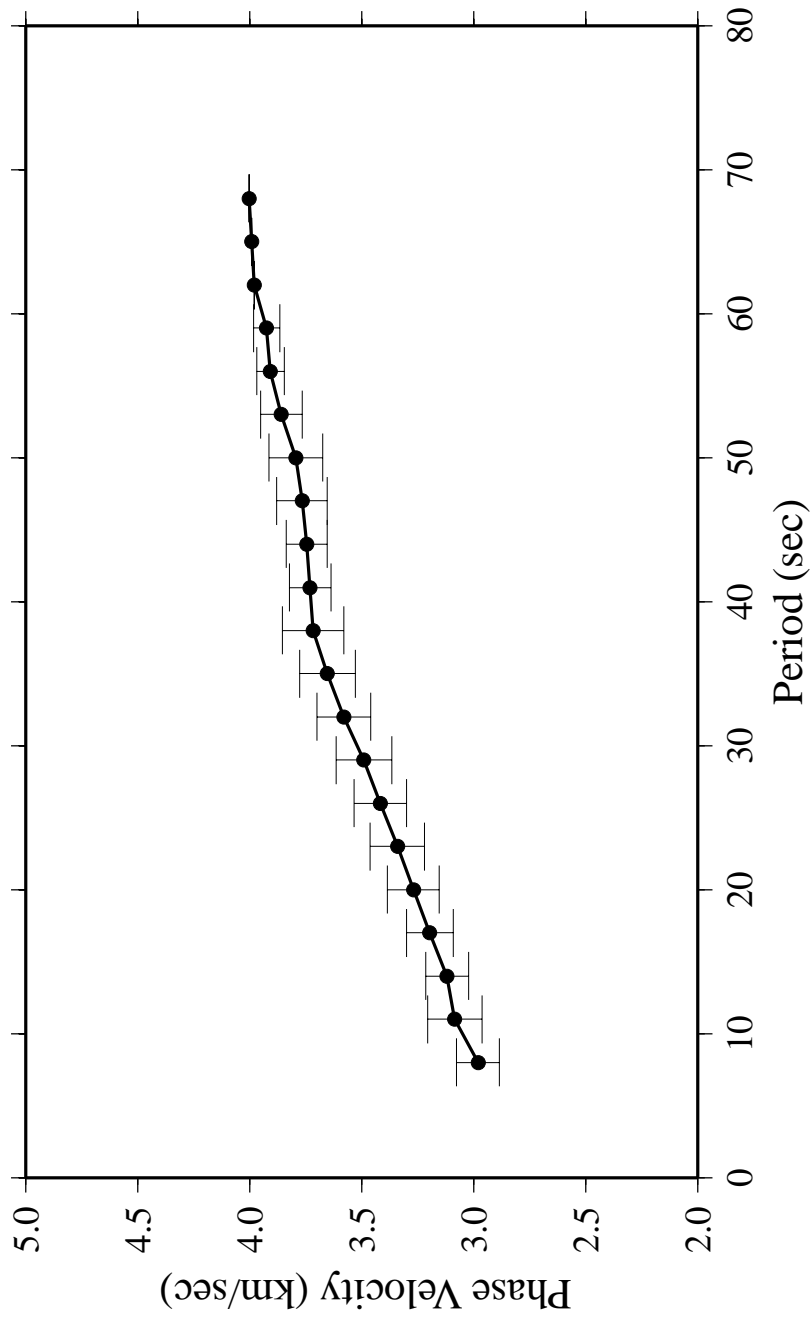


Figure 5.5.13. Observed Rayleigh-wave phase-velocities with calculated standard deviations for the Tarim-Tien Shan path.

this I assume an initial path length and phase velocity. Then the path length is changed by ± 10 km to examine the deviation from the assumed phase velocity. The results are shown in Table 3.

Table 3 Change in epicenter location and its affect on phase velocity.

Path Length	Observed Phase (seconds)	Phase Velocity (km/sec)	Error in Location (km)	Uncertainty (km/sec)
	100.0	2.5	+10	0.4
250 km	83.3	3.0	+10	0.12
	71.4	3.5	+10	0.14
	66.7	3.75	+10	0.09
	400.0	2.5	+10	0.25
1000 km	333.3	3.0	+10	0.03
	285.7	3.5	+10	0.035
	266.7	3.75	+10	0.04
	1200.0	2.5	+10	0.008
3000 km	1000.0	3.0	+10	0.01
	857.1	3.5	+10	0.012
	800.0	3.75	+10	0.013

As expected, longer source-receiver paths are less sensitive to epicenter location errors, whereas short paths are affected by small changes in epicenter location. This test shows good source locations are crucial for accurate estimates of phase velocities at short distances.

Another test was performed to understand how sensitive phase velocity is to changes in the strike, dip and rake of the source mechanism. The February 25, 1987 event recorded at WMQ had its source mechanism systematically changed by ± 10 for the strike, dip and rake. This event is part of the Tibet-Tarim Path located about 500 km from WMQ. Results show that at the long periods (> 50 seconds) there is a ± 0.1 km/sec change in the phase velocity with a corresponding change in strike. There is less of change in the phase velocity with the dip and almost no change with a change in rake. This may be an unusual path with little sensitivity, more work is needed before generalizing the results.

5.7 Estimating Earth Structure using Surface Wave Dispersion

Using all the estimated group and phase velocities from WMQ, a depth dependent shear-wave velocity structure is estimated with an inversion program called SURF (Herrmann, 1987, Russell, 1987). A stochastic damped least squares inversion was performed that minimizes the L2 norm of the misfit to the observations. The program evaluates the partial derivatives of the phase velocities

with respect to the layer shear velocity, compressional velocity, and group velocity. The inversion can be expressed as

$$d = G\delta m \quad (5.7.1)$$

where G is a matrix containing partial derivatives, d is a vector containing the observations (i.e. dispersion estimates), and δm is the correction vector of model parameters (i.e. shear-velocity model). Model parameters are perturbed from the initial guess of the model and fit to the observed values. If the size of the perturbations is kept small (by use of a damping factor) then the relation between the observable and parameter perturbation is linear (Aki and Richards, 1980).

Since the inversion suffers from non uniqueness, a priori knowledge of the region is needed to obtain a reasonable model. An existing shear-velocity model serves as a starting point in the inversions. There is no weighting of any particular layers in the inversion to allow the gross structure to become apparent. Iterations are monitored to minimize extraneous artifacts in the model (e.g. low-velocity zones). To obtain the best possible fit, the layer thicknesses are manipulated and another inversion is performed. In each initial model, thin 2.0 km layers are added to gain better resolution in the upper crust. The final model is chosen on how well it fits the observations and if the model is consistent with regional geology.

5.8 Damping Parameters for Shear-Velocity Inversion

A stochastic damped least squares inversion includes a damping factor that limits the amount of model variation between each iteration. During each iteration, the standard deviation between the observed and predicted models should reach a point where the change in the model is negligible (i.e. the model converges). The amount of damping affects how fast the model converges and the reduction in the standard deviation between the observed and predicted values. I tested different damping factors on the Mahdi and Pavlis initial model for the Tarim-Tien Shan path to see how damping affects the final model. High damping factors (e.g. >10.0) change the model slowly and takes more iterations to converge (e.g. 5) but produced a simpler, smoother model that fits the observed data. A damping factor of 5.0 converges faster (3 iterations), but introduced unnecessary complexity (i.e. small low-velocity zone) in the upper 5 km that does not fit geologic models for central Asia. Finally, a damping factor of 1.0 converges in the least amount of iterations (2) but

introduces a large low-velocity zone in the upper 5 km in the final model that is not geologically reasonable. Values below 1.0 converge within two iterations with similar results to using a damping factor of 1.0. For the inversions in this study, I use a conservative damping factor of 10 and monitor the iterations to insure that unnecessary artifacts (e.g. low-velocity zones) are not introduced into the final model.

CHAPTER 6 SEISMIC SHEAR-VELOCITY VARIATIONS OF CENTRAL ASIA

6.1 Shear Velocity for the Junggar Basin Path

Three models from previous studies were used as initial models in the inversion. The models include: The M1 model of Roecker et al. (1993), Mahdi and Pavlis (1998), and the Asia Earth model taken from Patton (1998). Each of these models incorporates a priori information such as regional geology and earthquake sources to help define layer thickness with depth. This information also provides constraints on where large increases in shear-velocities are likely to occur at depth. All of the model parameterizations were modified in the upper 15 km to try and improve flexibility in the upper crust by using thin 2.0 km thick layers. These small alterations do not affect the overall initial model, they allow more flexibility in the upper crust during the inversions.

During the inversion there several tools available to insure a good fit between the observed and predicted dispersion and shear-velocity models that aid in deciding when to stop iterating. The velocity dispersion mean error (V.D.M. in the tables) is the calculated by

$$\frac{1}{N} \sum \frac{(obs - predicted)}{residual} \quad (6.1.1)$$

where *obs* is the observed group or phase velocity at each period, *predicted* is predicted group or phase velocity of current model, *residual* is assumed error for each group or phase velocity (here I assume an error of 0.1 km/sec for each value chosen empirically from the epicenter relocation test) and N = the number of observations at each period. This calculation gives the overall fit between the observed and predicted dispersion velocities. The smaller this number, the better the observed velocities fit the predicted values. The standard deviation of the misfit is computed by

$$\sqrt{\frac{\sum (obs - mean)^2}{N - 1}} \quad (6.1.2)$$

where *obs* is the observed group or phase velocity at each period, *mean* is the mean of the observed velocities. The standard deviation shows the amount of scatter in the dispersion curves at

each period for the current model. If there is no standard deviation, then only one sample at that period exists. Weighted RMS is the root mean square between the observed and predicted group or phase velocities and is calculated by

$$\sqrt{\frac{\sum \frac{(obs - predicted)^2}{mean}}{N(n - 1)}} \quad (6.1.3)$$

where *obs* is the observed (initial) dispersion velocity, *predicted* is predicted dispersion value for the current model, *mean* is the mean calculated above, and *N* is the number of observations. Model length (model RMS) is the fit between the initial and final model values found in the same manner as the weighted RMS with the *obs* is the observed model shear velocities (from initial model) and *predicted* is perturbed model shear velocities for the current model.

As stated earlier, the inversion for the Junggar path includes three events with 47 observations. Results for the inversions are listed in Table 4. Final inversion models for the Junggar path are

Table 4 Parameters for Junggar Path Inversions

Model Name	Parameters	Initial Values (km/sec)	Final Values (km/sec)	No. Iterations
Central ASIA (Patton, 1998)	V.D.M.	-0.665	0.108	6
	Std. Err	2.23	0.888	
	Weighted RMS	1.65	0.661	
	Model Length	2.23	0.888	
Mahdi and Pavlis (1998)	V.D.M.	1.18	9.43e-2	6
	Std. Err	1.33	0.957	
	Weight RMS	0.970	0.699	
	Model Length	1.33	0.957	
M1 Roecker (1993)	V.D.M.	-1.20	1.01e-1	7
	Std. Err	2.17	0.812	
	Weight RMS	1.84	0.691	
	Model Length	2.17	0.812	

shown in Figures 6.1.1-6.1.3. Of the three initial models, the M1 initial model of Roecker et al., (1993) fits the observation the best. The standard deviation was reduced by 63% through 7 iterations. A low-velocity zone was introduced between 10 and 15 km and is probably an artifact of under-damping. At upper mantle depths, all of the final models are slower than the initial models.

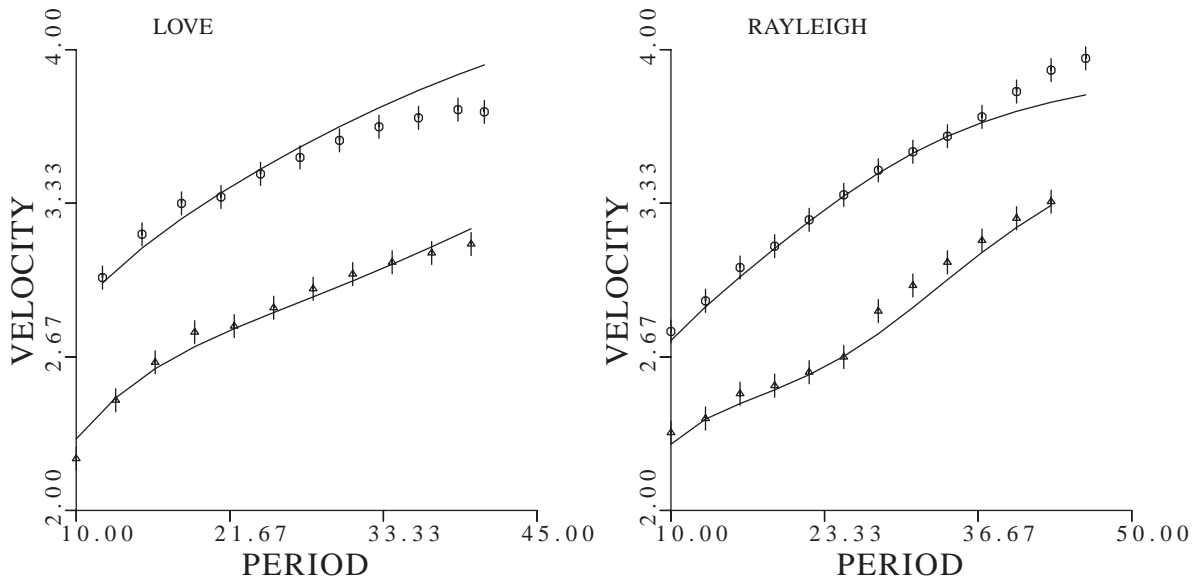
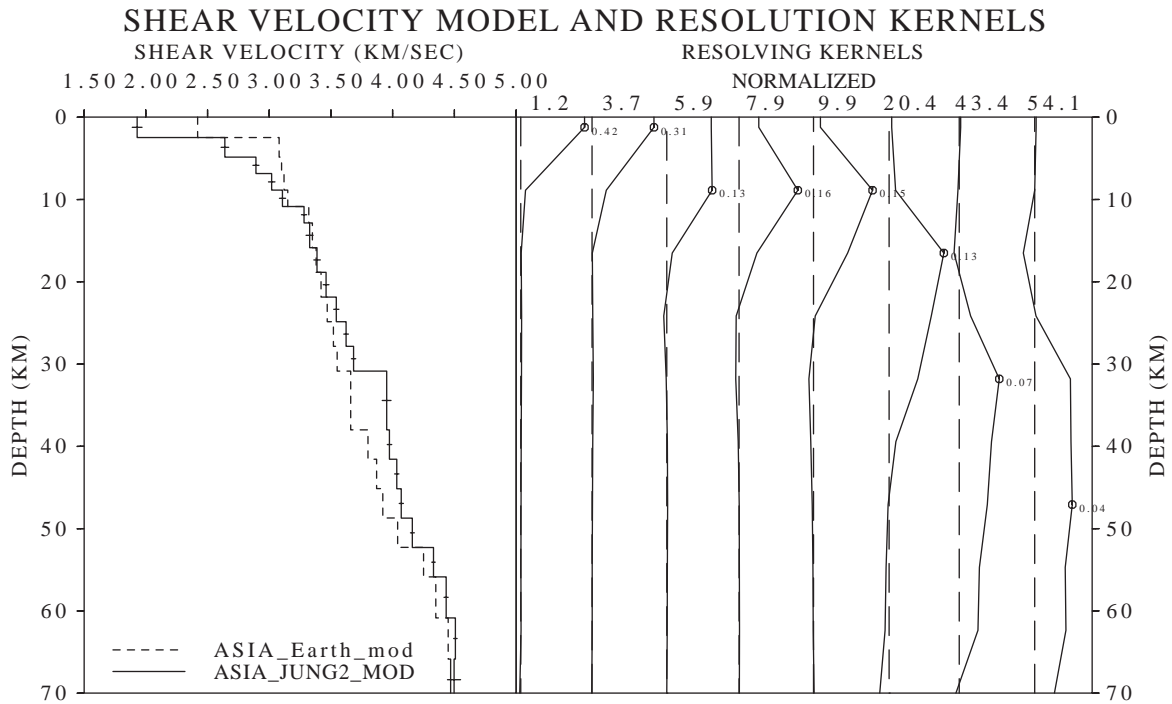


Figure 6.1.1. Inversion results for the Asia model of Patton (1998) for the Junggar Basin path. The top panel shows the final model and resolution kernels. The bottom diagrams show the fit of the observations to the predicted model. The top curve in each bottom diagram is the phase velocity fit to the model and the bottom is the group velocity fit (Rayleigh and Love).

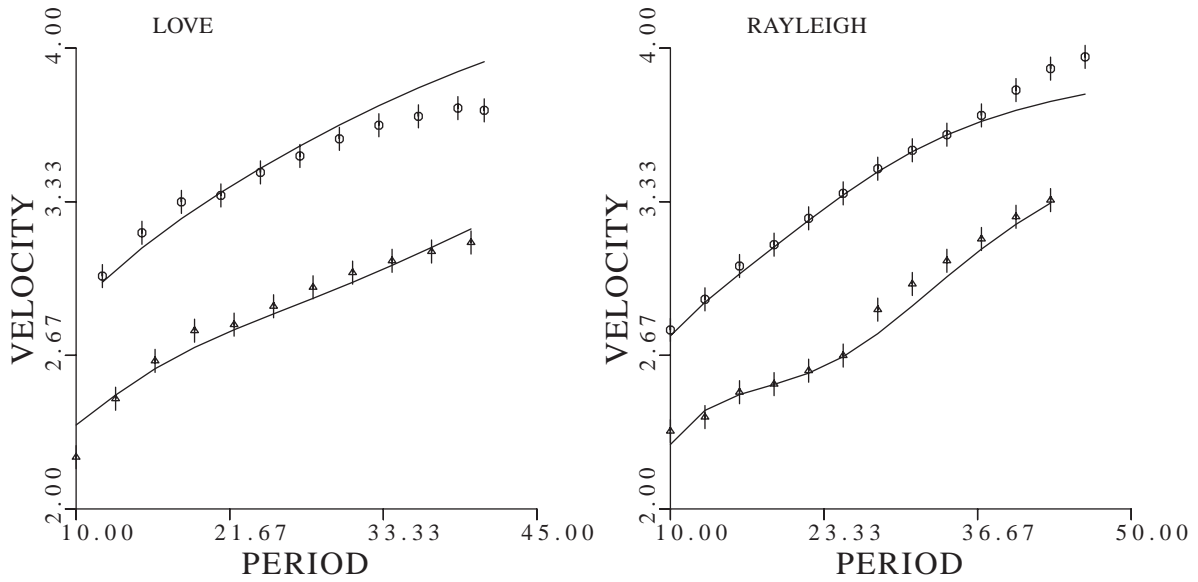
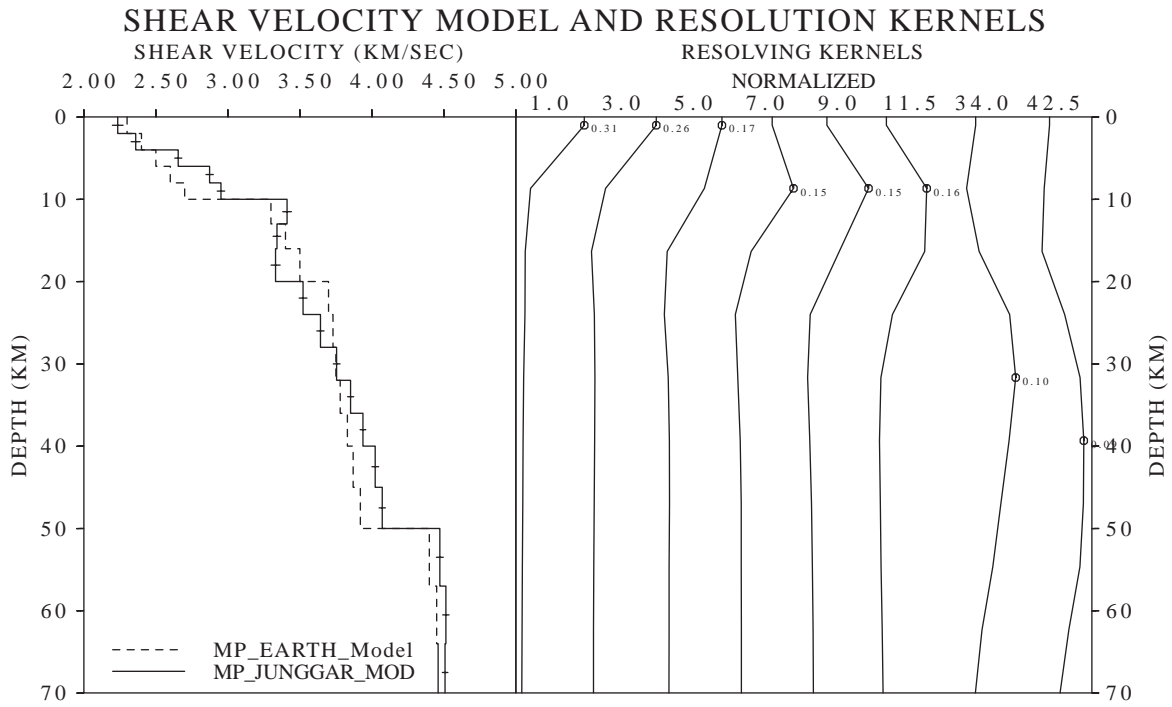


Figure 6.1.2. Inversion results for the Mahdi and Pavlis (1998) model for the Junggar path. See Figure 6.1.1 for explanation.

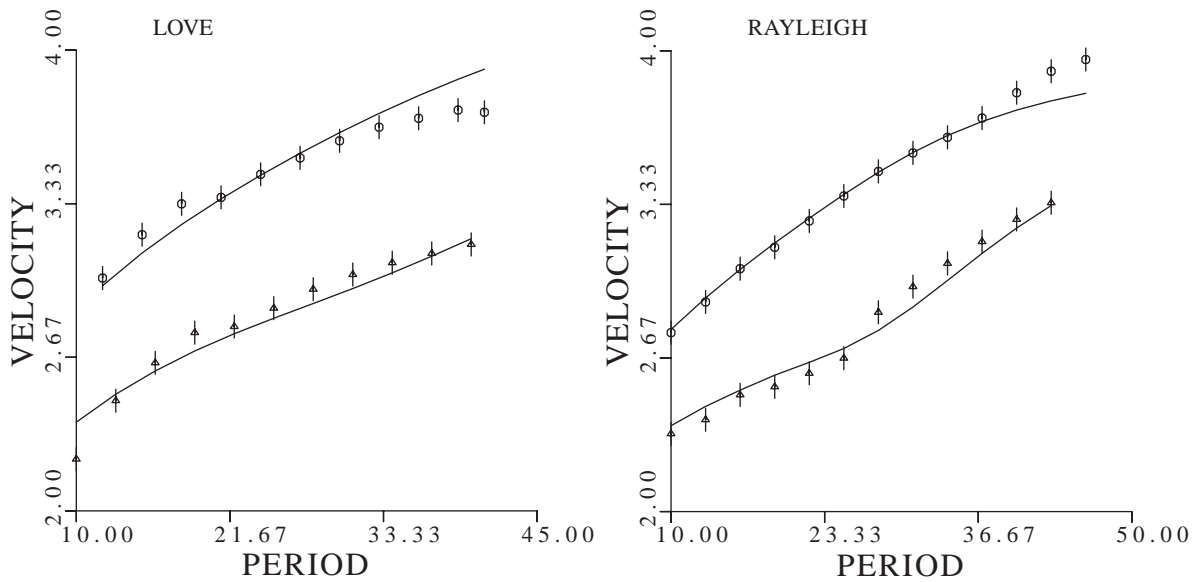
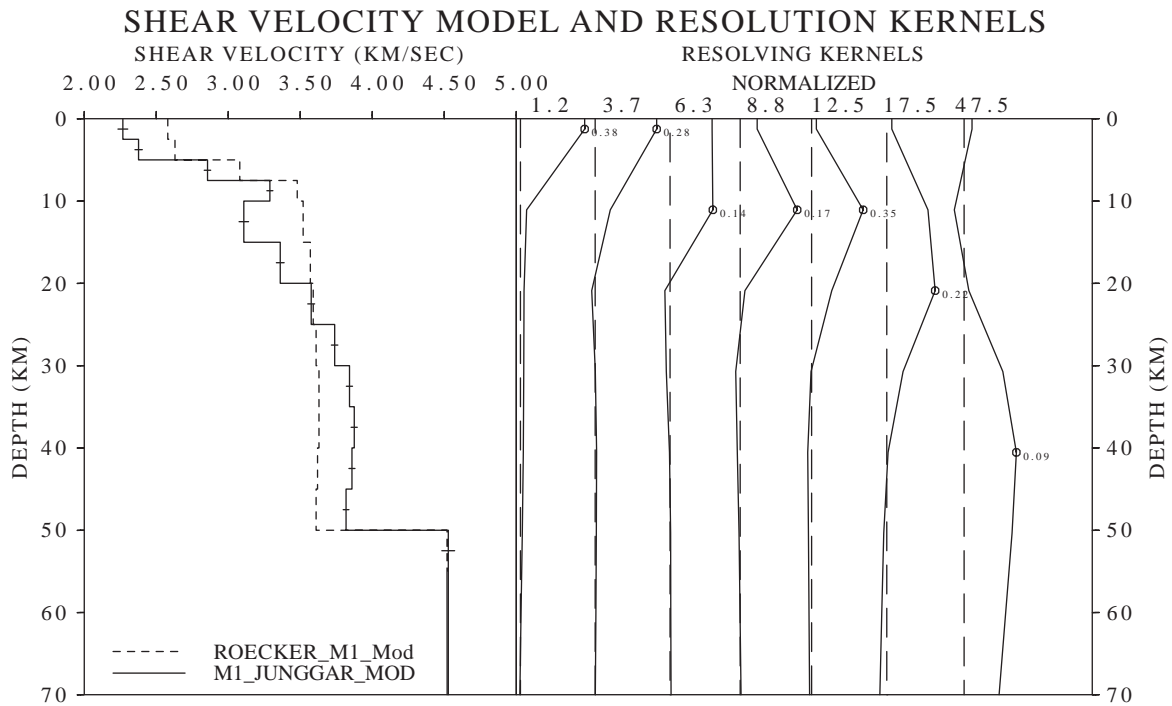


Figure 6.1.3. Inversion results for the Roecker et al. (1993) M1 model for the Junggar path. See Figure 6.1.1 for explanation.

6.2 Shear Velocity for the Tibet Plateau-Tarim Basin Path

As mentioned earlier, three events and 64 observations comprise the Tibet-Tarim Basin path. Parameters for the inversions are illustrated in Table 5.

Table 5 Parameters for Tibet-Tarim Path Inversions

Model Name	Parameters	Initial Values (km/sec)	Final Val- ues (km/sec)	No. Itera- tions
ASIA (Patton, 1998)	V.D.M.	1.08	5.80e-2	5
	Std. Err	0.963	0.842	
	Weighted RMS	0.789	0.691	
	Model Length	0.963	0.842	
Mahdi and Pavlis (1998)	V.D.M.	2.55	4.94e-2	6
	Std. Err	2.00	0.914	
	Weighted RMS	1.62	0.659	
	Model Length	2.00	0.814	
M1 Roecker (1993)	V.D.M.	0.381	4.09e-2	5
	Std. Err	0.891	0.855	
	Weighted RMS	0.795	0.763	
	Model Length	0.891	0.855	

After the inversions were performed, it was found that the best fit model corresponded to the Mahdi and Pavlis (1998) Tarim-Tien Shan initial model. All of the inversion results are presented in Figures 6.2.1-6.2.3. The upper 10 km of the final model is ~0.3 km/sec faster than the initial model. The mid-crustal depths (20-50 km) fit very well and the upper mantle velocities are slightly slower than the initial model. The standard deviation for the Tibet-Tarim Basin path was reduced by 59% through six iterations.

6.3 Shear Velocity for the Tarim-Tien Shan Path

The Tarim-Tien Shan path consisted of 8 events with 77 observations. Inversion parameters are shown in Table 6 for all three initial models. All of the inversion results are provided in Figures 6.3.1-6.3.3 and show that the Mahdi and Pavlis (1998) initial model best fits the observations. The standard deviation was reduced by 75% through five iterations. However, the other two models are not unreasonable except possibly at the upper crustal depths (< 10 km). A small low-velocity zone was introduced into the Mahdi and Pavlis model around 10 km depth and the M1 model around 15-20 km. This is maybe an artifact of overdamping and not a true geologic feat

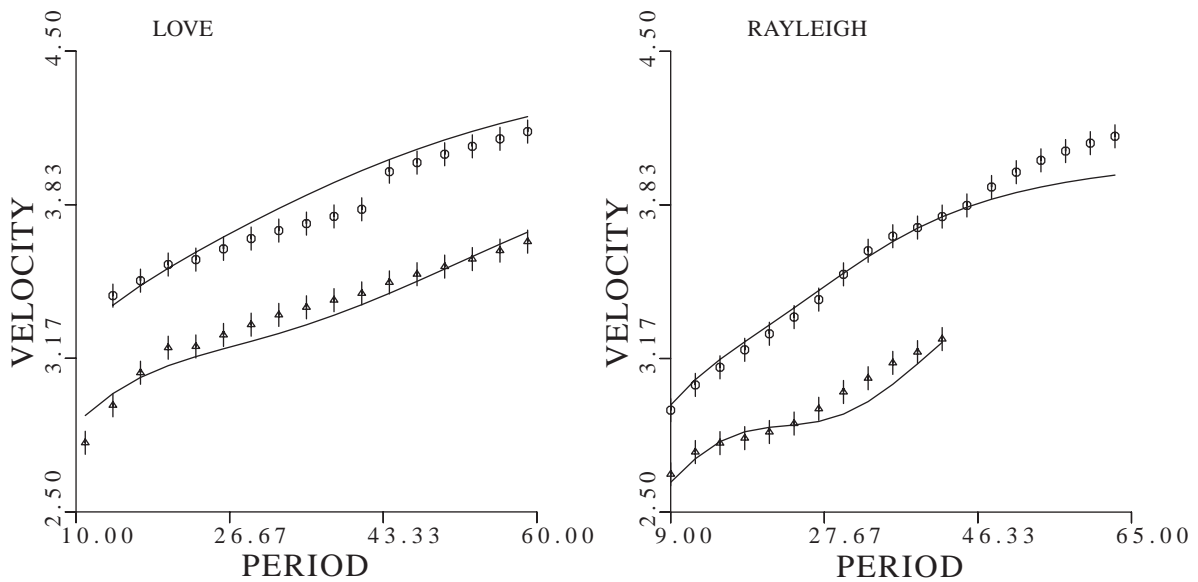
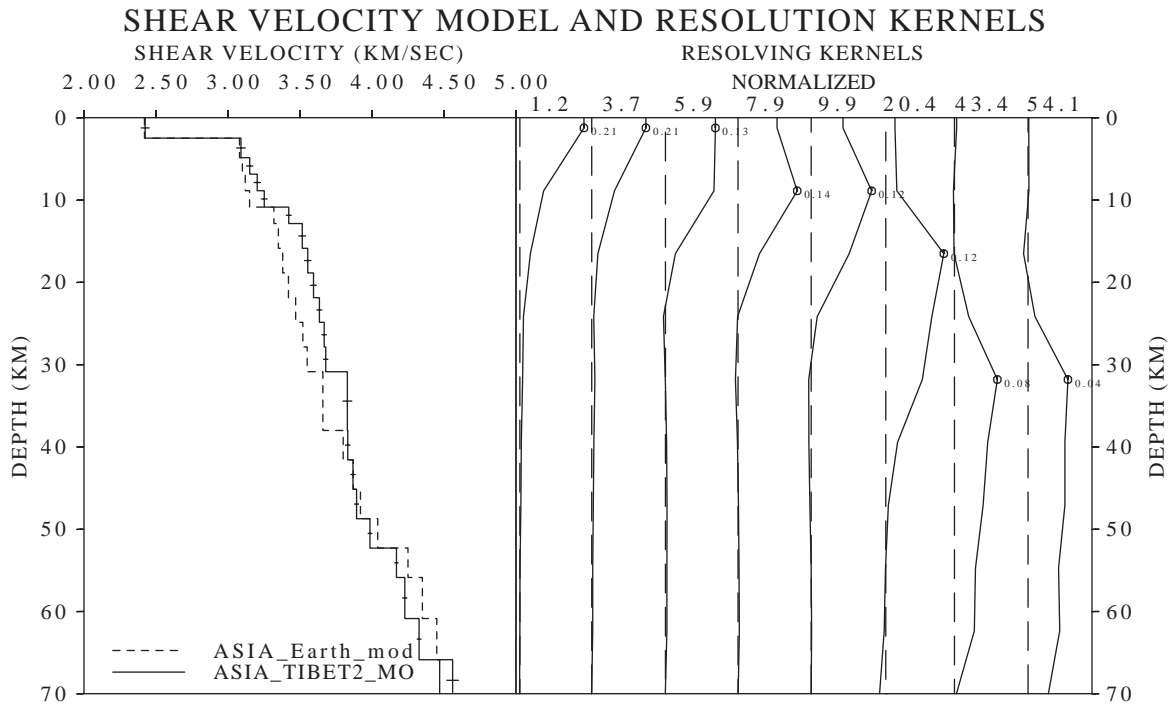


Figure 6.2.1. Inversion results for the Asia model of Patton (1998) for the Tibet-Tarim Basin path. See Figure 6.1.1 for explanation.

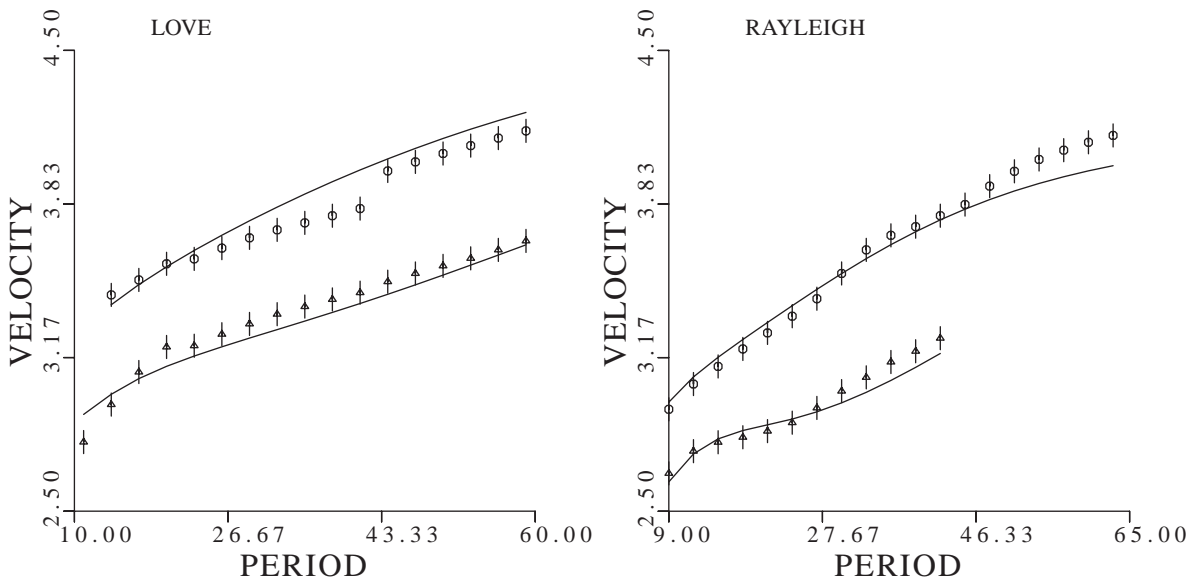
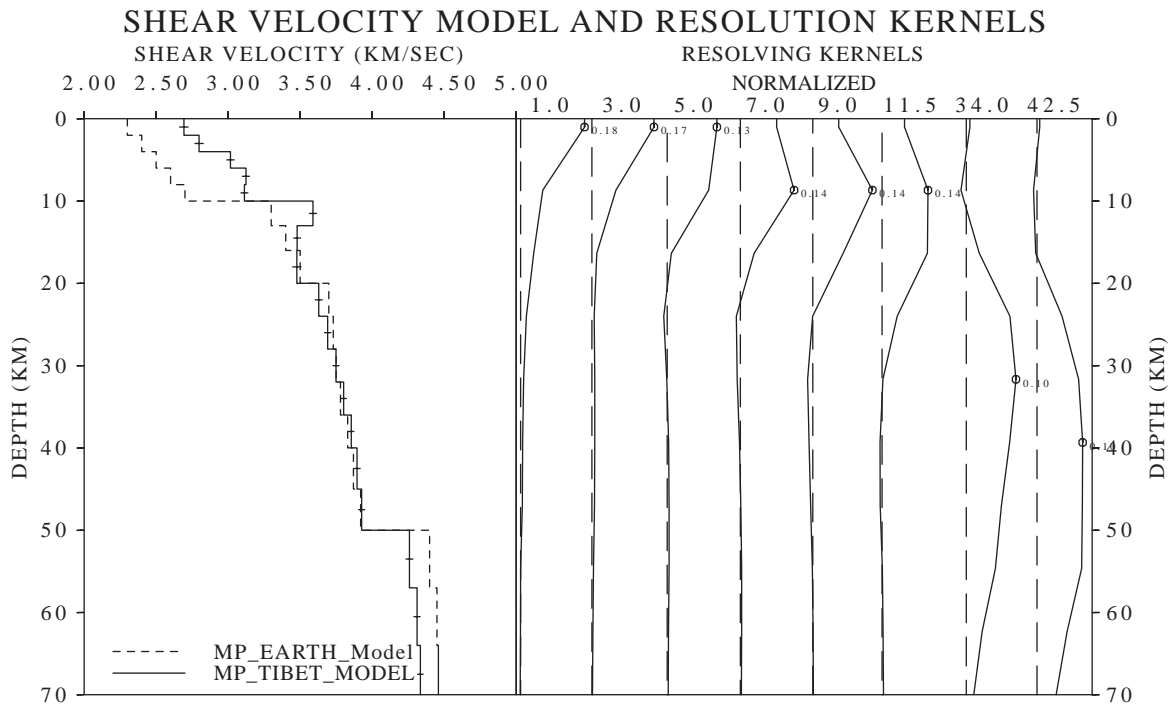


Figure 6.2.2. Inversion results for the Mahdi and Pavlis (1998) model for the Tibet-Tarim Basin path. See Figure 6.1.1 for explanation.

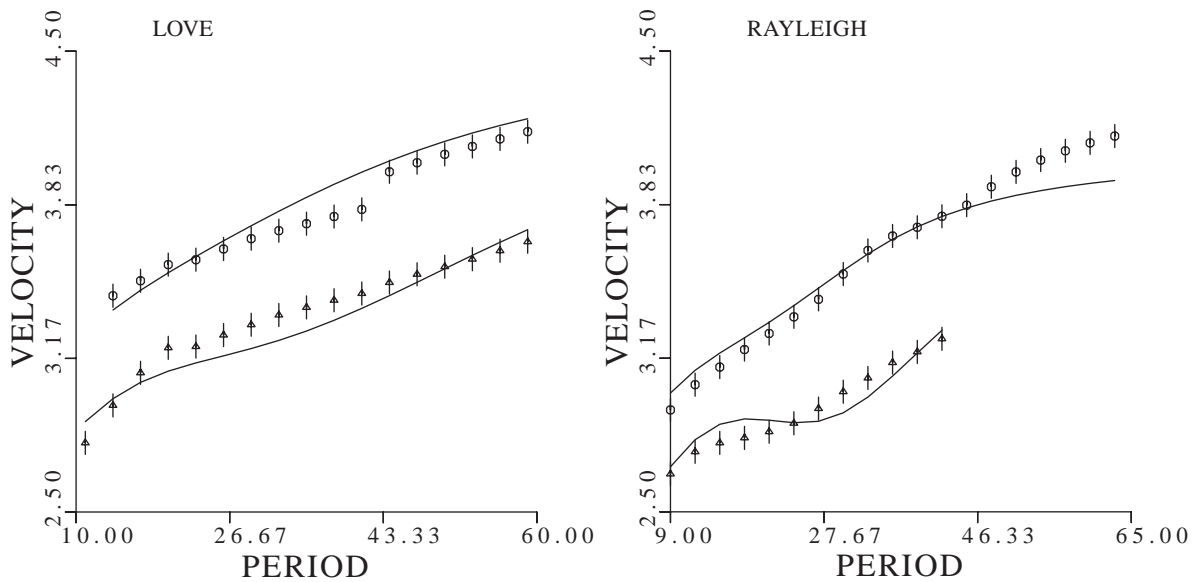
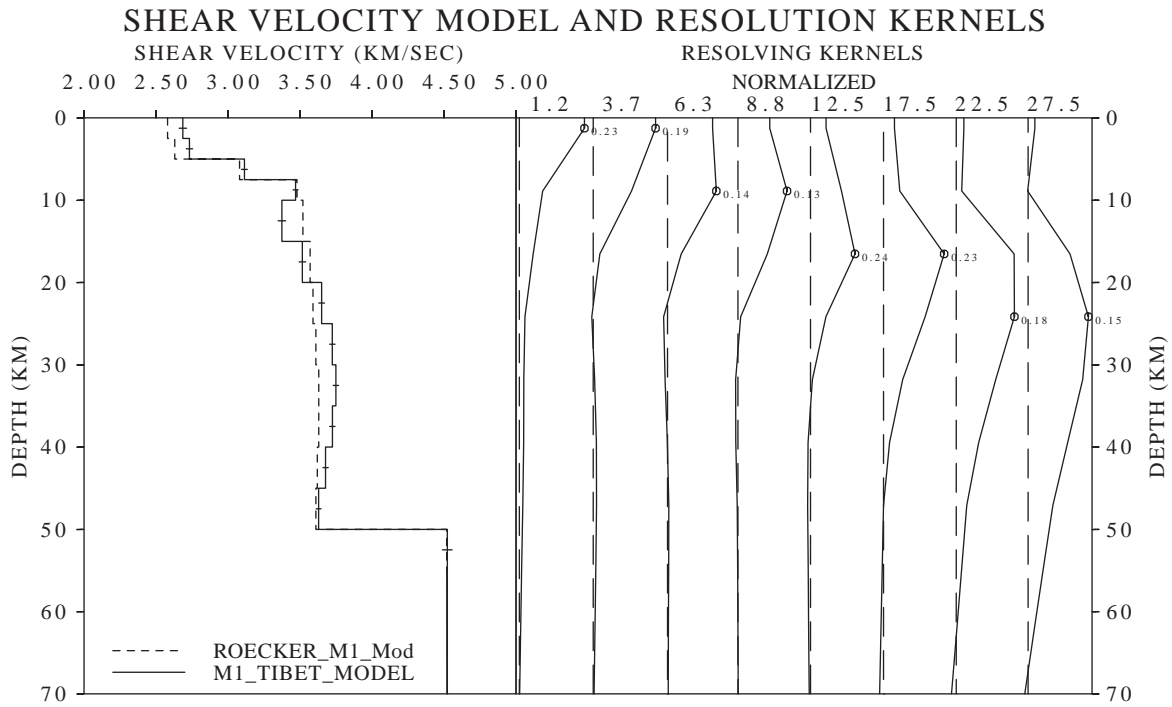


Figure 6.2.3. Inversion results for the Roecker et al. (1993) M1 model for the Tibet-Tarim Basin path. See Figure 6.1.1 for explanation.

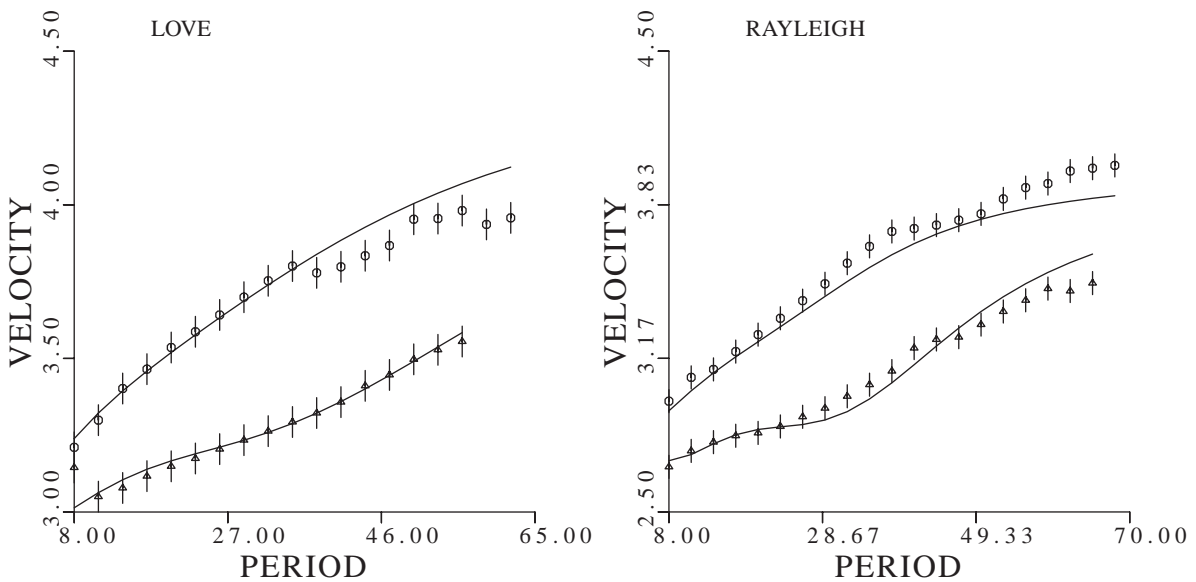
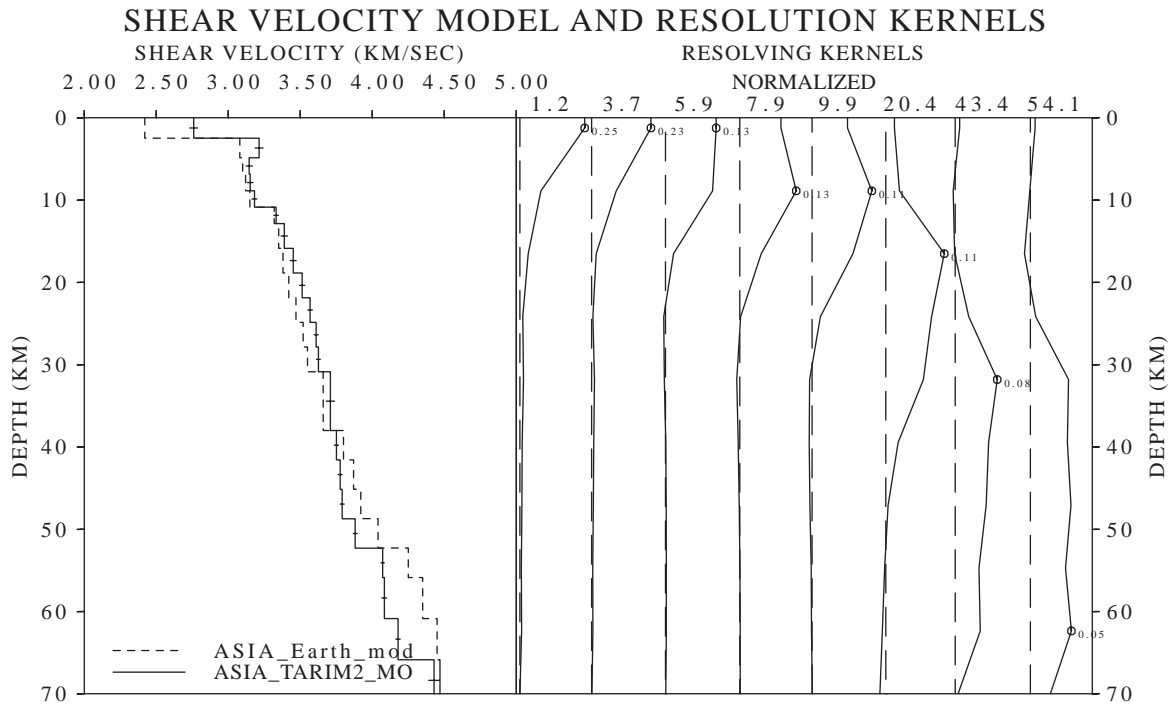


Figure 6.3.1. Inversion results for the Asia model of Patton (1998) for the Tarim-Tien Shan path. See Figure 6.1.1 for explanation.

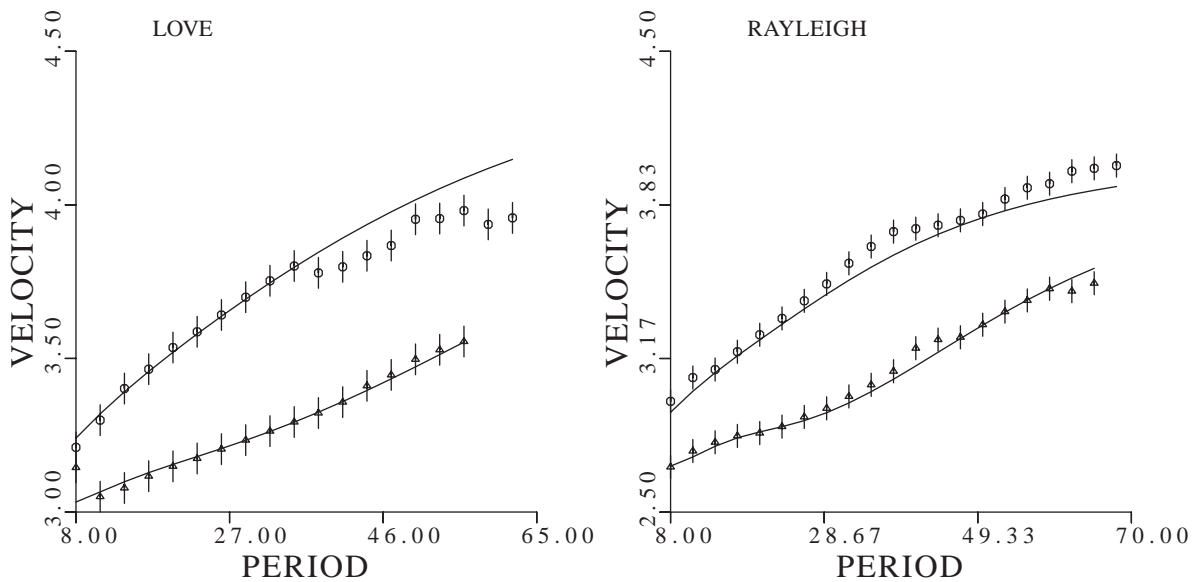
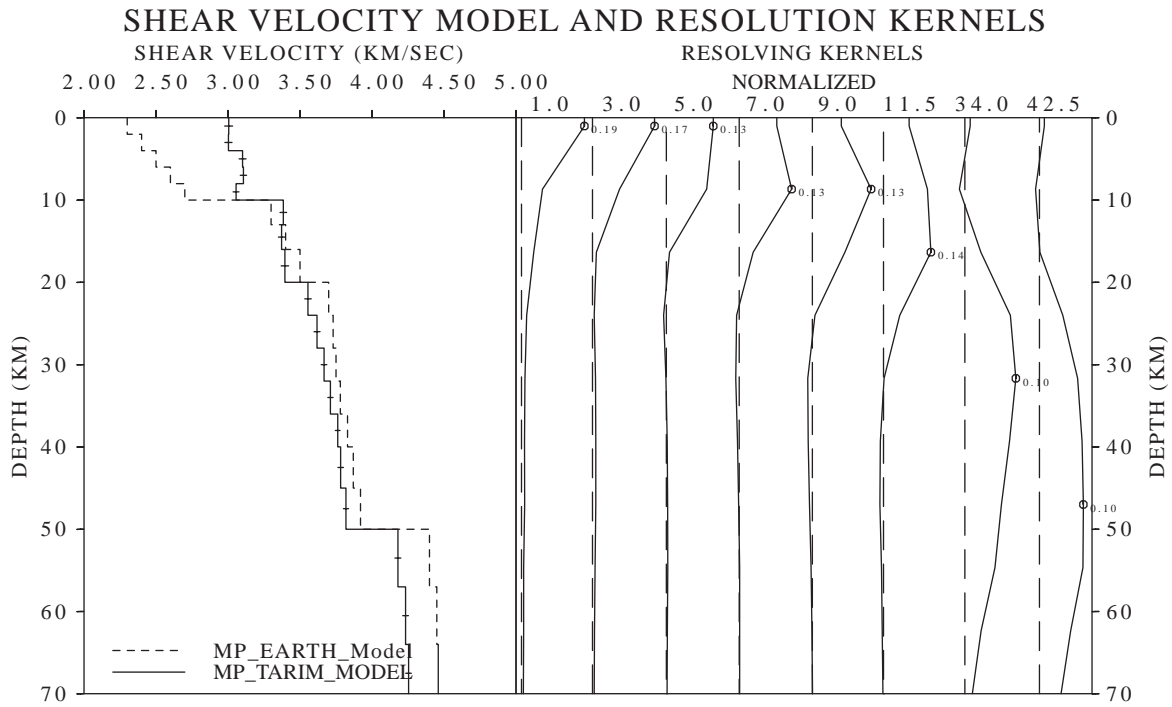


Figure 6.3.2. Inversion results for the Mahdi and Pavlis (1998) model for the Tarim-Tien Shan path. See Figure 6.1.1 for explanation.

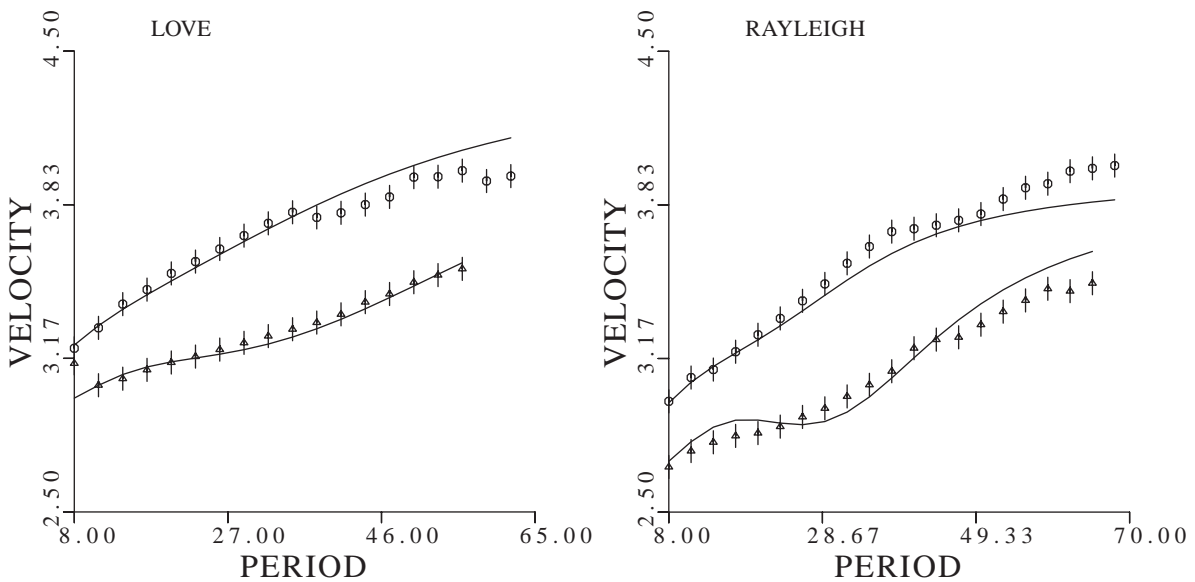
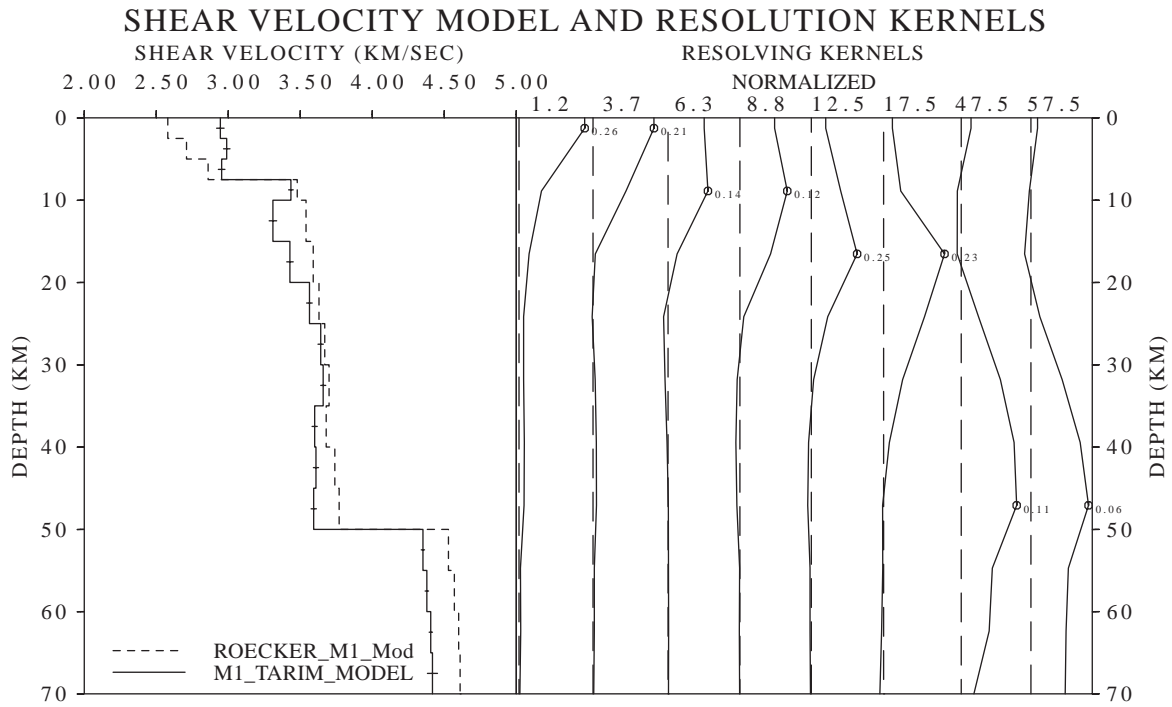


Figure 6.3.3. Inversion results for the Roecker et al. (1993) M1 model for the Tarim-Tien Shan path. See Figure 6.1.1 for explanation.

Table 6 Parameters for Tarim-Tien Shan Path Inversions

Model Name	Parameters	Initial Values (km/sec)	Final Val- ues (km/sec)	No. Itera- tions
ASIA (Patton, 1998)	V.D.M.	0.500	4.30e-2	6
	Std. Err	1.26	0.745	
	Weighted RMS	1.08	0.636	
	Model Length	1.26	0.745	
Mahdi and Pavlis (1998)	V.D.M.	2.09	5.96e-1	5
	Std. Err	2.60	0.668	
	Weighted RMS	2.19	0.565	
	Model Length	2.60	0.668	
M1 Roecker (1993)	V.D.M.	-0.308	2.39e-2	4
	Std. Err	1.46	0.777	
	Weighted RMS	1.30	0.691	
	Model Length	1.46	0.777	

CHAPTER 7 CONCLUSIONS

This is the only regional study of central Asia that incorporates both group and phase (Love and Rayleigh) simultaneously into a shear-wave velocity inversion. Previous studies have used either group or phase to invert for shear-velocity structures. The events used in this study were chosen because of their well constrained sources. Although there is no conclusive model that is going to be fully representing the shear-velocity structure of central Asia from these observations, there are important implications that come from this study.

In Figure 7.1.1 I show the upper 20 km of the crust of the best fitting models for each path. Both the Tarim-Tien Shan and Tibet-Tarim Basin models fit best with the Mahdi and Pavlis (1998) Tarim-Tien Shan initial model. Both the Tarim-Tien Shan and the Tibet-Tarim Basin paths have upper crust velocities significantly higher than the initial model. This discrepancy is probably a result of poor data at short periods. The Junggar Basin final model fits best using the M1 model of Roecker et al. (1993). There is a low-velocity zone between 10 and 15 km that is probably not a geologic feature but an artifact of the inversion process.

By using both group and phase estimate in the inversion, one can get a sense of how nonunique the modeling process is and that surface-wave dispersion alone is not sufficient to fully describe the geologic structure at depth. In addition, the observations from this study fit all the initial models with some degree of reasonability, which illustrates how all of the models may be viable for central Asia. The final models for each path show the observations are consistent with a 50-60 km thick crust. Crust and upper mantle shear-velocities are geologically reasonable and agree with both seismic and geophysical findings. The observations help constrain of the kind of model that can represent central Asia. Had the inversion initial models accounted for the variation in crustal thickness (i.e. 60 km beneath the Tien Shan; 50 km beneath the Tarim Basin; and 60 km beneath Tibet) the fit to the observations may have improved. The fits for the final models are still within reasonable geologic limits and again attest for the nonuniqueness of the inversion process.

As mentioned earlier, the initial model parameterizations were modified in the upper crust to allow the inversion some freedom. This is important because small nuclear detonations excite

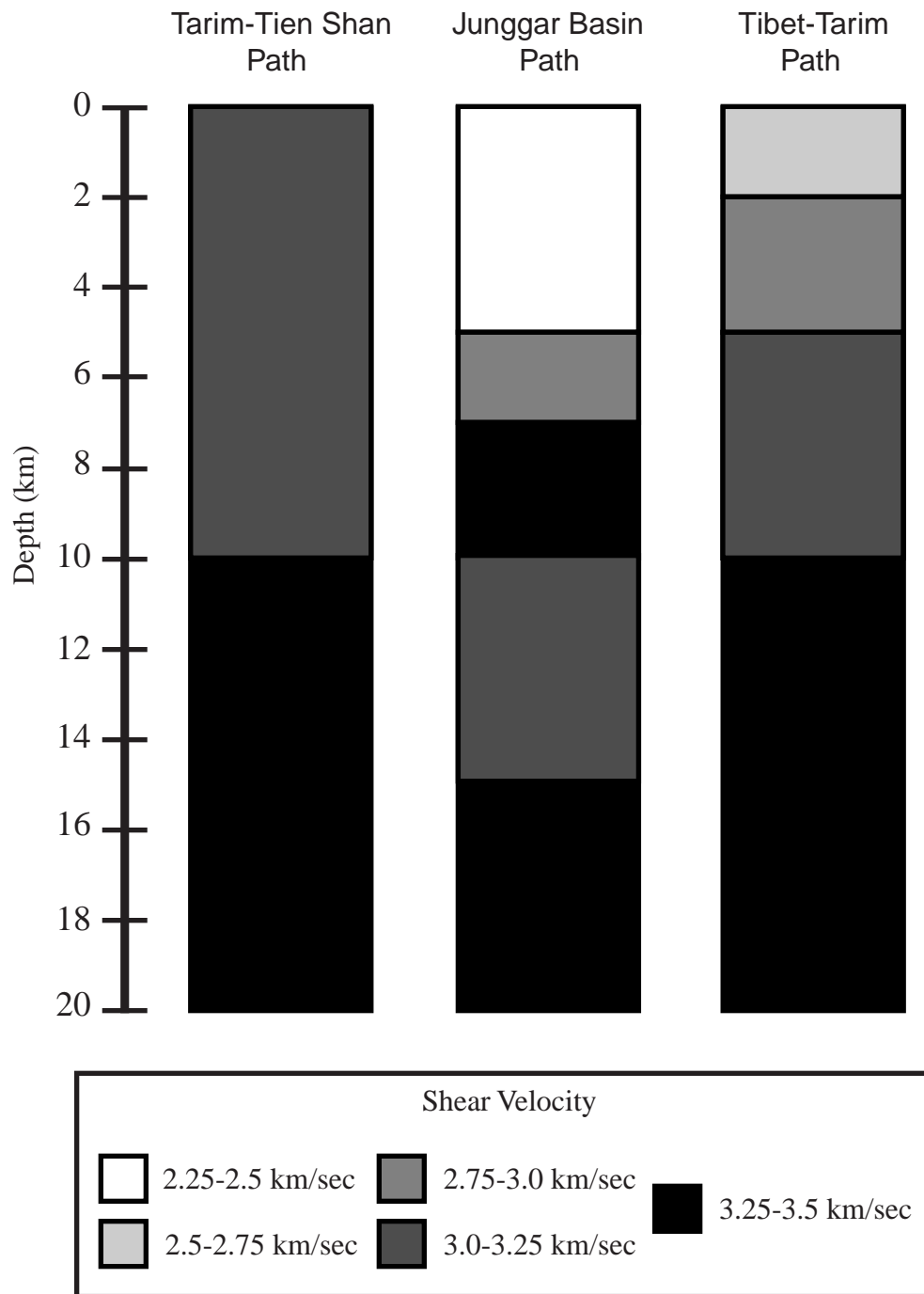


Figure 7.0.1. Final shear velocity models using the WMQ observations for the three paths. Only the upper 20 km is shown to illustrate resolution in the upper crust. The Tarim-Tien Shan and Tibet-Tarim Basin paths fit best with the Mahdi and Pavlis (1998) model; the Junggar Basin path fits best with the M1 model of Roecker et al. (1993).

short-period surface waves that are sensitive to the upper crust. By having thin upper crustal layers in the initial model, better resolution can be obtained for and help constrain source parameters for unknown seismic events (i.e. nuclear tests). To better constrain the upper crust, accurate data at the short-periods is needed in the inversions.

PARAMETERS FOR FINAL SHEAR-VELOCITY MODELS

Table 7 Final Shear-Velocity Model for the Tarim-Tien Shan Path

Layer Thickness (km)	P-wave velocity (km/sec)	S-wave Velocity (km/sec)	Density (g/cm ³)	Poisson's Ratio
2.00	5.09	3.00	2.52	0.23
2.00	5.25	3.00	2.55	0.26
2.00	5.33	3.10	2.57	0.24
2.00	5.37	3.11	2.57	0.25
2.00	5.32	3.06	2.56	0.25
3.00	5.84	3.38	2.66	0.25
3.00	5.75	3.37	2.65	0.24
4.00	5.92	3.39	2.68	0.25
4.00	6.16	3.55	2.74	0.25
4.00	6.27	3.62	2.78	0.25
4.00	6.35	3.67	2.80	0.25
4.00	6.42	3.71	2.83	0.25
4.00	6.51	3.76	2.85	0.25
5.00	6.55	3.78	2.86	0.25
5.00	6.62	3.82	2.88	0.25
7.00	7.22	4.18	3.05	0.25
7.00	7.33	4.23	3.09	0.25
7.00	7.36	4.25	3.10	0.25
7.00	7.41	4.28	3.11	0.25
7.00	7.45	4.31	3.12	0.25
10.0	7.43	4.29	3.12	0.25
0.00	7.92	4.57	3.28	0.25

Table 8 Final Shear-Velocity Model for the Tibet-Tarim Basin Path

Layer Thickness (km)	P-wave velocity (km/sec)	S-wave Velocity (km/sec)	Density (g/cm ³)	Poisson's Ratio
2.00	4.57	2.69	2.40	0.23
2.00	4.90	2.80	2.48	0.26
2.00	5.19	3.02	2.53	0.24
2.00	5.41	3.12	2.58	0.25
2.00	5.42	3.11	2.58	0.25
3.00	6.20	3.59	2.76	0.25
3.00	5.94	3.48	2.69	0.24
4.00	6.06	3.48	2.72	0.25
4.00	6.29	3.63	2.79	0.25
4.00	6.39	3.69	2.82	0.25
4.00	6.49	3.75	2.85	0.25
4.00	6.58	3.80	2.87	0.25
4.00	6.67	3.85	2.89	0.25
5.00	6.74	3.89	2.91	0.25
5.00	6.80	3.92	2.93	0.25
7.00	7.36	4.26	3.09	0.25
7.00	7.47	4.31	3.13	0.25
7.00	7.50	4.33	3.14	0.25
7.00	7.55	4.36	3.16	0.25
7.00	7.59	4.39	3.17	0.25
10.00	7.62	4.40	3.18	0.25
0.00	8.20	4.73	3.38	0.25

Table 9 Final Shear-Velocity Model for the Junggar Basin Path

Layer Thickness (km)	P-wave velocity (km/sec)	S-wave Velocity (km/sec)	Density (g/cm ³)	Poisson's Ratio
2.50	3.91	2.26	2.30	0.25
2.50	3.97	2.29	2.31	0.25
2.50	4.95	2.86	2.49	0.25
2.50	5.73	3.31	2.64	0.25
5.00	5.52	3.19	2.60	0.25
5.00	5.80	3.35	2.66	0.25
5.00	6.14	3.55	2.74	0.25
5.00	6.47	3.74	2.84	0.25
5.00	6.71	3.88	2.90	0.25
5.00	6.82	3.94	2.93	0.25
5.00	6.84	3.94	2.93	0.25
5.00	6.77	3.91	2.92	0.25
0.00	7.83	4.52	3.25	0.25

BIBLIOGRAPHY

Avouac, J. P., P. Tapponnier, M. Bai, H. You, and G. Wang, Active thrusting and folding along the northern Tien Shan and late Cenozoic rotation of the Tarim relative to Dzungaria and Kazakhstan, *J. Geophys. Res.*, 98, 6755-6804, 1993.

Bump, H.A., and A. Sheehan, Crustal thickness variations across the northern Tien Shan from teleseismic receiver functions, *J. Geophys. Res.*, 25, 1055-1058, 1998.

Burov, E.V., M.G. Kogan, H. Lyon-Caen, and P. Molnar, Gravity anomalies, the deep structure, and the dynamic processes beneath the Tien Shan, *Earth Planet. Sci. Lett.*, 96, 367-383, 1990.

Carroll, A.R., Y. Liang, S.A. Graham, X. Xiao, M.S. Hendrix, J. Chu, and C.L. McKnight, Junggar basin, northwest China: Trapped Late Paleozoic ocean, *Tectonophysics*, 181, 1-14, 1990.

Coleman, R.G., Continental growth of northwest China, *Tectonics*, 8, 621-635, 1989.

Cotton, F., and J. P. Avouac, Crustal and upper mantle structure under the Tien Shan from surface wave dispersion, *Phys. Earth Plan. Inter.*, 84, 1-4, 1994.

Der, Z., R. Masse, and M. Landisman, Effects of observational errors on the resolution of surface waves at intermediate distances, *J. Geophys. Res.*, 75, 3399-3409, 1970.

Ghose, S., M.W. Hamburger, and J. Virieux, Three-dimensional velocity structure and earthquake locations beneath the northern Tien Shan of Kyrgyzstan, central Asia, *J. Geophys. Res.*, 103, 2725-2748, 1998.

Hendrix, M.S., S.A. Graham, A.R. Carroll, E.R. Sobel, C.L. McKnight, B.J. Schuelein, and Z. Wang, Sedimentary record and climatic implications of recurrent deformation in the Tien Shan: Evidence from Mesozoic strata of the north Tarim, south Junggar, and Turpan basins, northwest China, *Geol. Soc. Am. Bull.*, 104, 53-79, 1992.

Herrin, E. and T. Goforth, Phase-matched filters: application to the study of Rayleigh waves, *Bull. Seismol. Soc. Am.* 63, 663-671, 1977.

Herrmann, R. B., Some aspects of band-pass filtering of surface waves, *Bull. Seismol. Soc. Am.*, 63, 663-671, 1973.

Herrmann, R. B., *Computer Method in Seismology*, St. Louis, University, St. Louis, MO, 1987.

Huang, T.K., J. Ren, C. Jian, Z. Zhang, and D. Quin, *Geotectonic evolution of China*, 203 pp., Springer-Verlag, New York, 1987.

Kosrov, G. L., N. V. Peterson, L. P. Vinnik, and S. W. Roecker, Receiver functions for the Tien Shan analog broadband network: Contrasts in the evolution of structures across the Talasso-Fergana fault, *J. Geophys. Res.*, 98, 4437-4448, 1993.

Mahdi, H. and G. Pavlis, Velocity variations in the crust and upper mantle beneath the Tien Shan inferred from Rayleigh wave dispersion: Implications for tectonic and dynamic processes, *J. Geophys. Res.*, 103, 2963-2703, 1998.

Molnar, P. and Q.D. Deng, Faulting associated with large earthquakes and the average rate of deformation in central and eastern Asia, *J. Geophys. Res.*, 89, 6203-6228, 1984.

Molnar, P. and P. Tapponnier, Active tectonics in Tibet, *J. Geophys. Res.*, 83, 5361-5375, 1978.

Nelson, M.R., R. McCaffery and P. Molnar, Source parameters for 11 earthquakes in the Tien Shan, central Asia, determined by P and SH waveform inversion, *J. Geophys. Res.*, 92, 12269-12648, 1987.

Ni, J., Contemporary tectonics in the Tien Shan region, *Earth Planet Sci. Lett.*, 41, 1978.

Patton, H. J., Measurements of Rayleigh-wave phase velocities Nevada: Implications for explosion sources and the Massachusetts Mountain earthquake, *Bull. Seismol. Soc. Am.* 72, 1329-1349, 1982.

Pavlis, G. and H. Mahdi, Surface wave propagation in central Asia: Observations of scattering and multipathing with Kyrgyzstan broadband array, *J. Geophys. Res.*, 101, 8437-8455, 1996.

Roecker, S.W., T. M. Sabitova, L. P. Vinnik, Y. A. Burmakov, M. I. Golvanov, R. Mamatkanova, and L. Munirova, Three-dimensional elastic wave velocity structure of the western and central Tien Shan, *J. Geophys. Res.*, 98, 15779-15795, 1993.

Russell, D. R., Multi-channel processing of dispersed surface waves, Ph. D. Dissertation, St. Louis Univ., St. Louis, MO, 1987.

Tapley, W. C. and J. E. Tull, 1992, SAC-Seismic Analysis Code. Regents of the University of California.

Tapponnier, P. and P. Molnar, Active faulting and tectonics of the Tien Shan, Mongolia, and Baykal regions, *J. Geophys. Res.*, 84, 3425-3459, 1979.

Vinnik, L. P., and A. M. Saipbekova, Structure of the lithosphere and the asthenosphere of the Tien Shan, *Ann. Geophys.*, 2, 621-626, 1984.

Zhang, Z.M., J.G. Liou, and R.G. Coleman, An outline of the plate tectonics of China, *Geol. Soc. Am. Bull.*, 95, 295-312, 1984.

Zonenshain, L.P., M.I. Kuzmin and L.M. Natapov, *Geology of the USSR: A Plate Tectonic Synthesis*, *Geodyn. Ser.*, vol. 21, edited by B.M. Page, 242 p., AGU, Washington, D.C., 1990.

VITA AUCTORIS

Brett Stephen Ketter was born on May 22, 1972, in Milwaukee, Wisconsin, U.S.A. The author attended the University of Wisconsin-Milwaukee from 1991-1996 as a geoscience major, receiving a Bachelor's degree in 1996. From 1997 to the present, the author has attended St. Louis University, studying in the Department of Earth and Atmospheric Sciences. He is currently engaged to be married in the summer of 1999.